공학박사학위논문

Structural Modifications of Some Nitrogen-containing Redox Couples for Improvement of Non-aqueous Flow Battery Performances

비수계 흐름 전지의 전기화학 성능 향상을 위한 질소를 포함하는 산화환원쌍의 구조 개선

2017년 2월

서울대학교 대학원

화학생물공학부

김 현 승

Abstract

As redox couples for non-aqueous flow batteries, the electrochemical and physicochemical properties of several nitrogen-containing molecules are examined. Nitrogen atom has lone pair electrons, which is applicable as ligand and redox center; thereby applying as redox couple design. Moreover, the negative charged nitrogen atom is nucleophile, resulting readily functional group substitution by S_N2 reaction. Thus, nitrogen atom can be applied as ligand molecule, redox center and the attachment center of aliphatic group for structural modification of redox couples. While non-aqueous flow battery is highlighted by its energy density from wide electrochemical stability window of organic electrolyte, the solubility drawback is remained problem for practical application of non-aqueous system. Since the nitrogen can be applied with diverse manner for molecule design, the limitation of solubility can be resolved by rational design of nitrogen-containing redox couples.

At first, an azamacrocyclic ligand-based complex cation, nickel(II)-1,4,8,11-tetraazacyclotetradecane (cyclam) is examined as a single redox couple for non-aqueous flow batteries. Single redox couple has advantageous feature for practical application because permanent loss of active material from cross-contamination at dual electrolyte-comprised cell is completely prevented. The energy density of this complex cation is tailored by easily dissociative counter anions and using highly dielectric solvents. The nickel(II)-chelated complex cation demonstrates high solubility (0.8 *M*) and working voltage (2.55 V) with bis(trifluoromethane)sulfonimide anion, resulting the energy density of 27.3 W h L^{-1}.

Secondly, nitrogen atom is used as two redox centers in *p*-phenyldiamines (PD) as positive redox couple. Two amine groups (-NH_2) in PD offers two redox reactions with single organic molecule. Thus, the demonstrated volumetric capacity from PD is twice higher than conventional one electron-involved redox couples at same concentration; thereby alloying cost advantages. Nevertheless, the solubility and chemical/electrochemical stability drawbacks are remained for flow battery applications in PD redox couple. Methyl substitution affects the solubility and chemical reversibility of redox couple because the methyl groups eliminates hydrogen bonding and shields foreign attack from electrolyte components. Fully-methyl substituted *N*,*N*,*N′*,*N′*-tetramethyl-*p*-phenylenediamine (TMPD) delivers high energy density with 938.0 W h L^{-1}, which is from 5.0 *M* of solubility and 3.2 and 3.8 V (*vs*. Li/Li^+) of working voltages. Furthermore, TMPD has facile diffusion rate, which is desirable for good rate capability.

Finally, butyl-substituted, *N*-butylphthalimide (BPI) is proposed as negative redox couple for non-aqueous flow batteries. The ten-fold increase of solubility (5.0 *M*) and decrease of melting point is from the less-packed asymmetric structure by attaching butyl groups on nitrogen atom. The strong correlation between maximum solubility and melting point implies this result. The electron-donating effect and solvation change of butyl groups shift the working voltage (0.1 V), resulting higher energy density. Consequently, BPI/TMPD comprised flow cell demonstrates promising electrochemical performance as all-organic flow batteries and the theoretical energy density of this cell is 120.6 W h L^{-1}.

The nitrogen-containing redox couple design is accomplished by directional approaching based on ideal solubility equation. Designed redox couples have higher energy density than conventional aqueous electrolyte ones; for instance, all-vanadium redox flow batteries, 25.0 W h L^{-1}. Thus, the high energy density non-aqueous flow batteries are designed by comprising nitrogen-containing molecules.

Keywords: Redox-flow batteries; Redox couples; Non-aqueous electrolytes; Solubility; Energy density; Electrochemical performances

Student number: 2012-22582

List of Figures

Fig. 10 FT-IR spectra of KBr-pelletized (a); cyclam, nickel(II) percholate and Ni(II)(cyclam)$[ClO_4]_2$ and (b); Ni(II)(cyclam)X_2 ($X = Cl^-, ClO_4^-$).

Fig. 11 (a); Orbital structure of Ni(II)(cyclam)Cl_2 and Ni(II)(cyclam)$[ClO_4]_2$. Cyclic voltammograms obtained from (b); 1 m*M* Ni(II)(cyclam)Cl_2 and (c); 10 m*M* Ni(II)(cyclam)$[ClO_4]_2$ dissolved 1.0 *M* $TEABF_4$ in AN supporting electrolyte. Scan rate = 100 mV s^{-1}

Fig. 12 (a); Molecular structure of Ni(II)(cyclam) and cyclic voltammograms from 10 m*M* Ni(II)(cyclam) dissolved 0.5 *M* $TEABF_4$ in EC/PC electrolyte for (b); Ni(II) to Ni(III) and (c); Ni(II) to Ni(I) redox reaction. Scan rates are indicated in the inset.

Fig. 13 (a); ln(i_p) *vs*. polarization plots and (b); calculated heterogeneous rate constants of Ni(II)(cyclam) and all-vanadium system

Fig. 14 (a); Scan-rate-dependent cyclic voltammograms with electrochemical stability window of supporting electrolyte and (b); 1^{st} and 50^{th} repeated voltammograms of Ni(II)(cyclam). Scan rate for supporting electrolyte = 10 mV s^{-1}.

Fig. 15 (a); Sweep segments from cyclic voltammetry on platinum-coated quartz crystal electrode surface and (b); mass change of inert electrode traced by EQCM at Ni(II)(cyclam) dissolved electrolyte. Scan rate = 300 mV s^{-1}

Fig. 16 Cyclic voltammograms recorded from 0.4 *M* Ni(II)(cyclam) dissolved 0.5 *M* $TEABF_4$ in EC/PC (1:1 = *v*/*v*) at (a); Ni(II) to Ni(III) and (b); Ni(II) to Ni(I). (c); Randles-Sevcik plots from Ni(II)(cyclam) redox reactions. The scan-rate-

dependent peak current values are obtained from (a) and (b).

Fig. 17 Exploded view of homemade H-cell

Fig. 18 (a); Accumulated capacity *vs*. cell voltage curves recorded from 10 m*M* Ni(II)(cyclam) dissolved 1.0 *M* $TEABF_4$ in EC/PC (1:1 = *v*/*v*) electrolyte at carbon paper/TEA^+ exchange membrane/carbon paper comprised H-cell. H-Cell was charged to SOC 30 and fully discharged (0.0 V voltage cut). (b); Cycleability of Ni(II)(cyclam) dissolved electrolyte and (c); 1^{st} Differential capacity plot from (a). Currents are 0.3 *C* and 0.15 *C* CC for charging and discharging, respectively.

Fig. 19 (a); cyclic voltammograms obtained from 10 m*M* Ni(II)(cyclam) dissolved 1.0 *M* $TEABF_4$ in EC/PC (1:1 = *v*/*v*) electrolyte at carbon paper inert electrode. (b); Chronopotentiogram recorded at H-cell GITT experiment and (c); calculated concentration ratio at inert electrode surface from QOCVs. Current and rest period for GITT experiment are 10 min (current = 0.3 *C* CC) and 20 min, respectively. (d); Coin-type cell cycling at 50 μA cm^{-2}. Voltage cut-off = 2.0~2.7 V.

Fig. 20 (a); Ionic radius of various anions and (b); solubility and working voltage of Ni(II)cyclam complex cation with various counter anions at 1.0 *M* $TEABF_4$ EC/PC (1:1 = *v*/*v*) supporting electrolyte

Fig. 21 (a); 10^{th} and 50^{th} cyclic voltammograms obtained at 10 m*M* Ni(II)(cyclam)$[TFSI]_2$ dissolved 1.0 *M* $TEABF_4$ in EC/PC (1:1=*v*/*v*) supporting electrolyte. (b); time *vs*. voltage curves from modified coin-cell

List of Tables

Contents

1. Introduction

Electricity becomes more important with the increase of global energy consumption [1]. Therefore, the cost and environmental issues from the fossil fuel-based power plants are must be resolved by introduction of renewable energy resources [2]. Nevertheless, the intermittent energy supply from renewable resources (*e.g.* solar) and non-equivalent usage of electricity in the daytime and nighttime are still remained problems at the distributed-level for efficient usage. Since the energy storage systems (ESS) stores energy and discharges when it is needed, control of electricity is possible by comprising ESS as a compartment of power plants. The large-scale ESS, therefore, can be a solution for those problems. Among the several suggested ESS systems, the secondary battery-based ESSs are highlighted from its high stability and reliability. To comprise battery system as a vital system of ESS, however, safety, cost and cycleability issues must be improved. It is because the fluctuation of electricity usage is near periodical in the year-round and the basis energy and power of ESS is massive from this electricity usage. Hence, advanced non-lithium based batteries such as redox-flow batteries (RFB) are suggested to overcome those problems in ESS. RFB is promising battery candidate for ESS by following characteristics: *i*) long service life from no mechanical degradation of electrode material, *ii*) lower cost per energy than conventional secondary batteries [3].

Typical secondary batteries are composed with four essential compartments. Positive and negative electrode (inert or not inert), separator (single-ion conductor or porous polymeric film) and electrolyte are those four elements. Among those four parts,

electrolyte is a key determinant compartment for improving battery performances and systems [4]. RFB is an example for this occasion. RFB stores energy by dissolved redox couples at both electrolyte side and two inert electrode at positive and negative side are comprised as inert electrode in stack. Since heterogeneous charge transfer (electron tunneling) at the electrode surface is the main charge/discharge mechanism of RFB, the electrochemical performances of RFB are mainly determined by physicochemical and electrochemical properties of used electrolyte solution. Thus, the chemical and electrochemical properties of electrolyte solutions are directly correlated with battery performances. Dissolved redox couple is one of the most important determinants for electrolyte performances. Especially, to achieve advanced energy density and electrochemical performances of RFB system, the brand-new design principle for redox couple is needed for high solubility with reliable stability and working voltage.

Since the 1950s, redox flow battery systems have prospered with aqueous solvent based system [5]. However, there are several drawbacks to the use of an aqueous solvent: *i*) working voltage of the assembled cell with 1.23 V from the electrochemical stability window of water, theoretically and *ii*) highly corrosive electrolyte solution with concentrated sulfuric acid, especially all vanadium redox flow batteries (VRBs). In order to deal with these issues, a non-aqueous solvent based RFB can be used [6]. When an organic solvent is used as an electrolyte in the RFB system, the working voltage of the cell is almost twice higher than when it is under the aqueous system and non-corrosive electrolytes can be produced. Nevertheless, the currently suggested

redox species has some practical limitations to be an electrolyte of a non-aqueous flow batteries. The most important drawback is the concentration of active species which directly correlates with the theoretical volumetric capacity of electrolyte. By W. Wang *et al.*, previously reported active material cases commonly have solubility with less than 0.1 *M* at acceptable supporting electrolyte concentration (larger than 1.0 *M* of salts) [7]. Therefore, to achieve a greater energy density with non-aqueous electrolytes, highly soluble redox couples in non-aqueous solvents are urgently needed.

The possible redox couples for non-aqueous flow battery electrolyte are largely divided in two categories. The first is transition metal-centered redox couples [8]. Several transition metal-ions are stabilized with ligand molecules and demonstrate stable oxidation states of center metals. Since the charging and discharging of electrolyte are the redox reactions of dissolved redox couples, these metal-centered redox couples can be applied as active materials for RFBs. Previously demonstrated complexes are mostly bidentate ligand-based couples [9, 10]. However, those redox couples demonstrate restricted electrochemistry at alkyl ammonium-based salts and show limited solubility at used solvents [11]. To achieve both economical advantage and high solubility, organic redox couples is comprised as active materials [12]. The second type of redox couple demonstrates high solubility at carbonate-based supporting electrolyte. Nevertheless, several couples still have low solubility [13] and the candidates for organic RFB system is limited from the complicate redox chemistry.

To realize non-aqueous supporting electrolyte based RFB system, the design principle for high energy density redox couple is crucial. If we can develop proper design

principle for enhancing energy density of redox couples, more improved physicochemical and electrochemical properties of redox couples can be achieved. This rule-of-thumb not only improves the performances of already reported couples, but also suggests new redox couples for RFB electrolytes. In this study, therefore, to improve energy density and electrochemical performances of non-aqueous RFB system, the thermodynamic parameters for redox couples are used as barometer for volumetric capacity (solubility of redox couple). Furthermore, the electrochemical characteristic of redox couples is tailored by introducing functional groups or alternating counter anions. Several improved nitrogen-containing redox couples based on design principle are proposed as the high energy density redox couples for non-aqueous flow batteries. Furthermore, the improved physicochemical/electrochemical characteristics for those redox couples are to determine whether those improved compounds satisfies the redox couples for non-aqueous RFBs.

2. Background

2.1. Electrochemistry and electrochemical methods

Electrochemistry refers to the relationship between electron and chemical species. Electrochemical reaction involves electrode and chemical species and the oxidation is defined as releasing electron from chemical species to electrode and reduction is gaining electron from electrode. This electrochemical reaction can be summarized as below:

$$R \rightarrow O + ne \text{ (oxidation)}$$

$$O + ne \rightarrow R \text{ (reduction)}$$

Since the mechanism of charge transfer is governed by quantum tunneling, the electrochemical reaction only takes place at the near surface of used electrode. This charge transfer (electron transport) is occur when the electrode potential is higher or lower than energy level of highest occupied molecular orbital (HOMO) and lowest unoccupied molecular orbital (LUMO) of electrolyte solution, respectively; for instance, reduction occurs that electrode potential is negative than LUMO of electrolyte. Therefore, we can address electrode potential as energy level of electron in electrode. **Figure 1** demonstrates relationship between electron energy level of electrode and electrolyte. Moreover, transferred rate of electron at electrochemical reaction is observed as current. Thus, the current expresses rate of electrochemical reaction. An electrochemical cell is composed with at least three compartments.

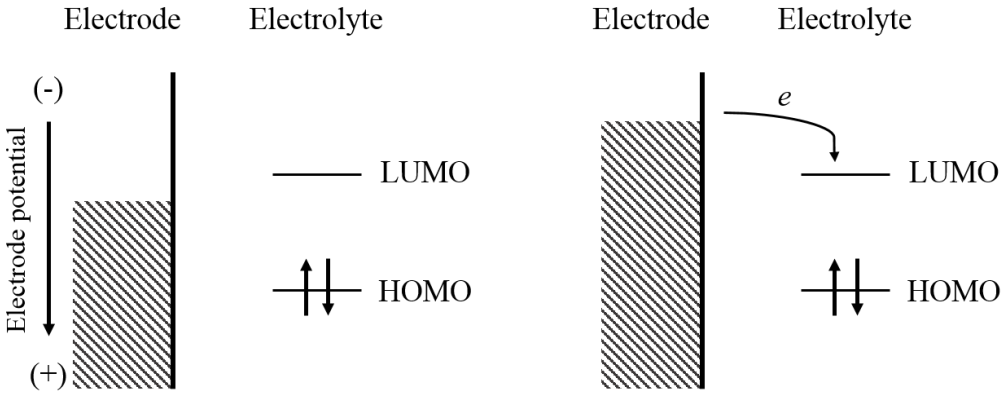

Fig. 1 Electron energy of electrode and heterogeneous charge transfer

Working electrode, counter electrode and electrolyte are those three. Since current flows with electrochemical reaction, equivalent value of current must flow at counter electrode and electrolyte for charge compensation. In electrochemistry, therefore, this closed-loop must be satisfied. **Figure 2** demonstrates this closed-loop in electrochemical cell. Note that reduction takes place at cathode and oxidation occurs at anode surface.

If electrochemical system is thermodynamically and electrochemically reversible, the system follows Nernst equation. According to Nernst equation based on half-cell reduction potential:

$$E_{red} = E_{red}^{0} + \frac{RT}{nF} \ln \frac{a_O}{a_R}$$

where, E_{red} is reduction potential of half-cell at certain temperature, R is gas constant (8.314 J K^{-1} mol^{-1}), T is temperature, n is the number of equivalents of electron transferred, F is Faradaic constant (96485 C mol^{-1}) and a is activity of redox species. Note that E_{red}^{0} is reduction potential at standard condition. From Nernst equation, we can define the concentration ratio of redox couples in electrolyte solution because the potential is variated with concentration ratio change of redox couples.

The standard reaction Gibbs free energy (ΔG^o) of half-cell reaction also can be described:

$$\Delta G^o = -nFE^o$$

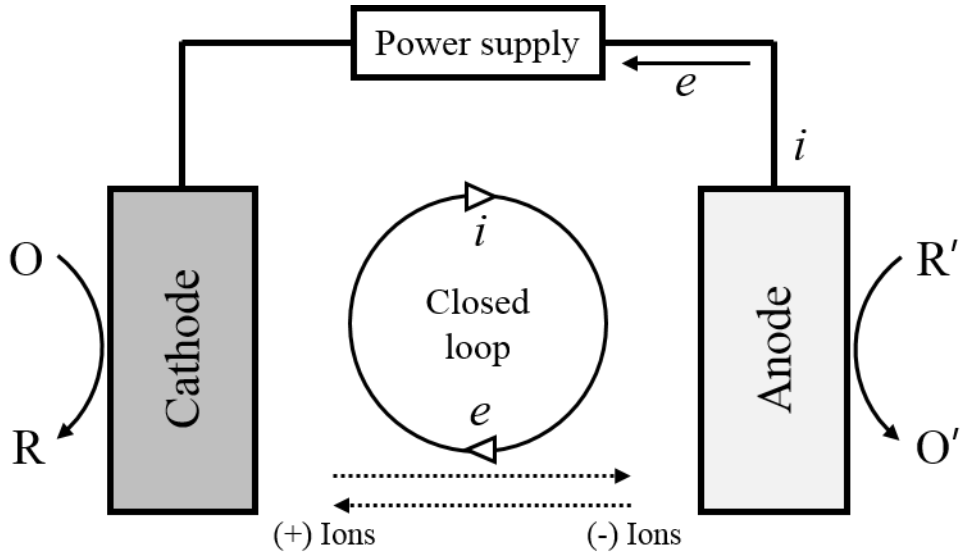

$$i_c = |i_a| = i(electrolyte)$$

Fig. 2 Closed-loop in electrochemical cell

where, n is the number of equivalents of electron transferred, F is Faradaic constant (96485 C mol^{-1}) and E^0 is standard reduction potential. Two half-cells can be selected to compose full cell for electrochemical reaction. Therefore, to achieve high cell voltage, two half-cells with very negative (positive) electrode potential should be selected. If the total Gibbs free energy of full cell is negative, a spontaneous electrochemical reaction is observed in this cell. This system is called galvanic cell. In contrast, at the positive total Gibbs free energy, additional electric energy is required for proceeding electrochemical reaction (electrolytic cell).

Since, secondary battery system is electrolytic cell at charging and galvanic cell at discharging, the round-trip efficiency (energy efficiency) of cell must be lower than 100% even at fully electrochemically and chemically reversible system. It is because energy loss by polarization is inevitable during electrochemical reaction. The charging voltage (voltage at charging, E_{chg}) and working voltage (voltage at discharging, E_{wk}) can be described as:

$$E_{chg} = E_{cell} + (\eta_a + \eta_c + iR_{total})$$

$$E_{wk} = E_{cell} - (\eta_a + \eta_c + iR_{total})$$

where, η_a is activation overpotential, η_c is concentration overpotential, i is applied current and R_{total} stands for total series resistance of electrochemical cell. The equation clearly indicates that the polarization loss (sum of each overpotentials and iR_{total} loss) of electrochemical cell is detrimental factor for efficient usage of energy in secondary

battery. To enhance energy efficiency of cell, the application of electro-catalysts and decrease in series resistance of cell is definitely important. Hence, the proper cell design is crucial for better electrochemical performance of secondary batteries. For instance, increase of cell area reduces cell resistance at same ionic conductivity, thereby allowing the lower polarization than smaller cells, resulting better energy efficiency or power at same applied current.

2.2. Thermodynamics of melting and its effect on solubility

Electrolyte for RFB is composed of supporting electrolyte (salt and solvent) and redox active species. Therefore, the volumetric capacity of RFB is largely determined by both concentration of salt and redox couples. It is because the capacity of electrolyte is not only determined by the amount of electron stored in electrolyte, but also the charge compensation by generation of closed-loop in the cell. Since the maximum concentration of salt in organic solvents is as high as 2.0 to 5.0 *M* [14], the crucial determinant of volumetric capacity in non-aqueous RFB is the maximum concentration of redox couples. However, the solubility of redox couple is very limited in typical organic solvents (less than 0.1 *M*) [7]. Therefore, to overcome this solubility (volumetric capacity) drawback in non-aqueous electrolytes, the fundamental understanding of dissolving process is essential.

Dissolution of solute molecule is firstly in progress with the disappearance of interaction between solute molecules. Therefore, the overall interaction strength of solute molecules are the major factor for maximum solubility of solute molecules. The

empirical study reveals that the melting point of solute solid is well-correlated with the interaction strength of between molecules. Based on the idea of interpreting interaction strength of solid by melting point, the ideal solubility is predicted by:

$$x_{solute} = e^{\left[-\frac{\Delta H_f}{R}\left(\frac{1}{T_{solvent}}-\frac{1}{T_m}\right)\right]}$$

where, x_{solute} is the mole fraction of the solute molecules in the solution, ΔH_f is the enthalpy of fusion of solute, R is the universal gas constant (8.314472 J K^{-1} mol^{-1}), $T_{solvent}$ stands for the temperature of solvent and T_m is the melting point of the solute. Equation states that the lower T_m and ΔH_f are favorable for high solubility.

Furthermore, at the phase transition of solid molecule, the melting point is strongly correlated with heat of fusion. Heat of fusion can be stated as the sum of total interaction between solid molecules. Therefore, the type of secondary interaction is definitely important for high solubility. Since Gibbs free energy at phase transition is zero value, the melting point can be expressed as heat of fusion divided by heat of entropy. In summary, thermal properties of solid at phase transition can be stated as:

$$\Delta H_f = \sum n_i m_i$$

$$T_m = {\Delta H_f}\Big/{\Delta S_f}$$

where n_i is the number of group i, m_i is the contribution of group i to the enthalpy of

fusion, and ΔS_f is the entropy of fusion of solid. m_i is the highest at typically strong hydrogen bonding [15]. Thus, the type of secondary bonding is important for achieving high solubility. Therefore, weak van der Waal interaction is favorable for highly soluble redox couples in terms of melting point and heat of fusion.

2.3. Redox-flow batteries

Redox-flow batteries (RFB) are firstly proposed by A.M. Posner at 1955 with Sn/Br or Fe dissolved electrolyte [5]. The active material of RFB is redox couple dissolved electrolyte solution. Since the electrode is inert at both charging and discharging of RFB, physical degradation of electrode is totally absent in principle. Thus, long-term cycleability is expected at RFB system by this reason, theoretically. Furthermore, RFB stores electricity at electrolyte reservoir (electrolyte tank) and the charge transfer takes place at the electrode stack. Therefore, energy density and power density of RFB can be designed respectively [7]. From this characteristic, the easiness of battery design can be expected at RFB. The total battery capacity is easily controlled by the size of tank and concentration of redox couples from this distinct characteristic of RFBs. In RFB system, therefore, the cost per energy (kW h) is being economical with high capacity system [3]. Thus, RFBs are considered as distributed-leveled energy storage system. **Figure 3** demonstrates schematic illustration for RFB system. Cell voltage of RFB can be controlled by selecting both proper supporting electrolyte and redox couple. It is because practical usage of redox couple is determined by electrochemical stability window of supporting electrolyte. Two types of supporting electrolytes are mainly

suggested for RFB system. Aqueous and Non-aqueous electrolyte are those two. Since the 1950s, RFB have prosper with aqueous supporting electrolyte based systems [16]. However, electrochemical stability window of aqueous solvent limits the working voltage of aqueous RFB by lower than 1.23 V. This practical drawback leads RFB to non-aqueous supporting electrolyte-based system. When salt dissolved non-aqueous solvent is used as supporting electrolyte, the limitation of working voltage is largely resolved. However, the solubility problem (lower than 0.1 *M*) is major bottle-neck for this system [7].

2.3.1. Aqueous flow batteries

Water is one of the most common solvents and it can be applied as a solvent for RFB system. The most common forms of aqueous supporting electrolytes are sulfuric acid or hydrochloric acid dissolved water solvent. Iron-chromium (Fe/Cr) based RFB is one of the early systems and developed in NASA [17]. Two redox reactions for Fe/Cr RFB is described as below:

Positive electrolyte: $Fe(III) + e \leftrightarrow Fe(II)$, $E^0 = 0.77$ V (*vs*. SHE)

Negative electrolyte: $Cr(III) + e \leftrightarrow Cr(II)$, $E^0 = -0.41$ V (*vs*. SHE)

Since two different redox couples are used as positive and negative electrolyte respectively, the cross-contamination of electrolyte leads battery to degradation of

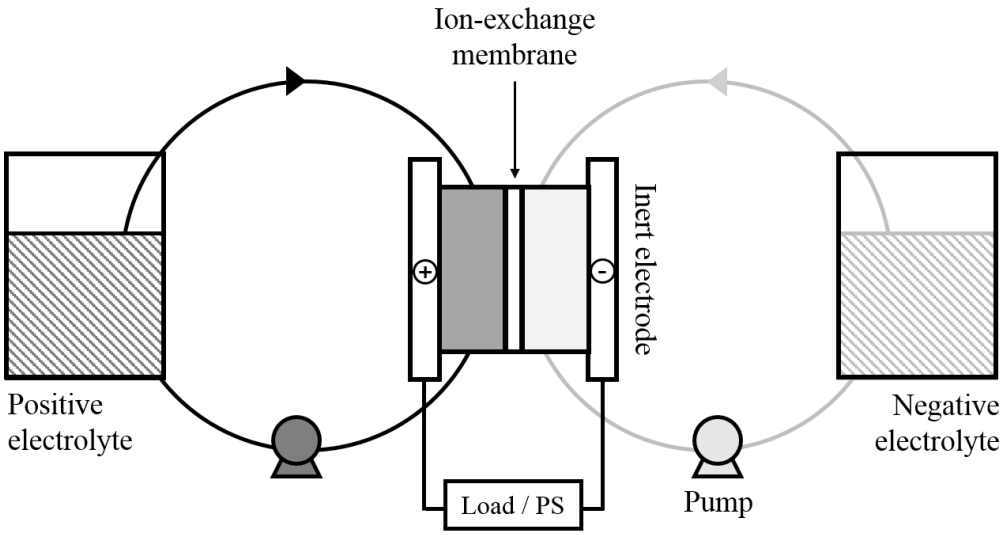

Fig. 3 Redox-flow batteries

Coulombic efficiency and permanent loss of redox couples. To countermeasure this problem, the single redox couple based system is suggested. All-vanadium RFB is such example. This system is firstly proposed by M. Skyllas-Kazacos at 1986 [16, 18]. The beneficial feature of all-vanadium system is long-term cycleability of RFB. Therefore, all-vanadium system is considered as promising distribution-leveled energy storage system. Positive and negative half-cell reactions are addressed as below.

Positive electrolyte: $VO_2^+ + 2H^+ + e \leftrightarrow VO^{2+} + H_2O$, $E^0 = 1.00$ V (*vs*. SHE)

Negative electrolyte: $V(III) + e \leftrightarrow V(II)$, $E^0 = -0.26$ V (*vs*. SHE)

Though electrochemical reaction at negative electrolyte is acceptably facile enough, redox reaction at positive electrolyte is slow from its complicate electrochemistry [19]. Therefore, catalyst for positive electrolyte is widely suggested [20-22]. The problematic feature of all-vanadium system is temperature dependency of vanadium salts. Vanadium(V) oxide precipitation is easily formed above 50 ℃ with 5 *M* of sulfuric acid at positive electrolyte [23]. Therefore, the energy density of this system is restricted by solubility (less than 1.8 *M*). To resolve this problem, organic and inorganic electrolyte additives are suggested for stable electrolyte solution. Furthermore, from its cell voltage (1.26 V), the gradual loss of electrolyte solution is detrimental factor for battery stability.

Zinc-bromine (Zn/Br) RFB is one of the early aqueous electrolyte-based systems, which is already commercialized. Charge and discharge mechanism for Zn/Br RFB is:

Positive electrolyte: $Br_3^- + 2e \leftrightarrow 3Br^-$, $E^0 = 1.09$ V (*vs*. SHE)

Negative electrolyte: $Zn(II) + 2e \leftrightarrow Zn^0$, $E^0 = -0.76$ V (*vs*. SHE)

Since Zn/Br RFB have potential leakage risk from the toxicity of Br_2, the complex agent for bromine is developed (*i.e.* quaternary ammonium salts) [24]. The evolution of Br_2 quite degrades Zn/Br battery. The reduction potential of dissolved Br_2 is 1.09 V (*vs*. SHE). Thus, the self-discharge of plated zinc metal is spontaneously occurred by Br_2 generation. The electrode gap between positive and negative electrode side is separated by porous separator from this reason. The electrochemical kinetics of positive and negative electrolyte redox reactions are very different. While the redox reaction of zinc plating and dissolution is facile, the oxidation of bromine is not quite rapid. Therefore, the kinetics of electrochemical reactions must be balanced. In general, the surface area of inert carbon electrode is higher at the positive electrolyte side. The dendritic formation of zinc is also observed at Zn/Br RFB. However, the dendritic form of zinc cannot penetrate the separator [25]. From the cost-effectiveness, this Zn/Br RFB is practically applied as load leveling applications.

2.3.2 Non-aqueous flow batteries

To enhance working voltage and complicate electrochemistry of aqueous system, non-aqueous supporting electrolyte based RFB is suggested. By using organic supporting electrolytes, three advantageous features can be accomplished, theoretically. First, the high working voltage can be achieved because typical organic solvents used in

electrochemical experiment have electrochemical stability window higher than 3.0 V. Therefore, the working voltage of unit cell can be enlarged higher than 1.23 V. Second is the wide applicable electrode candidates from non-corrosive organic electrolytes. Aqueous RFB uses highly acidic corrosive electrolyte for electrolyte stability and conductivity. From this corrosive nature, the metal electrode cannot be used as electrode material by metal dissolution. However, in the non-aqueous electrolyte, wide metal and metal oxide materials can be applied as electrode at both positive and negative sides. Further decrease in polarization is possible by electro-catalytic effects. The last advantageous feature is less temperature dependency. For instance, propylene carbonate solvent is at liquid in the temperature range of -48.8 to 242.0 ℃. Therefore, carbonate solvent-based electrolyte can demonstrate stability with no site-dependency. ESS is a massive battery system and the installation places of ESS are various with applications. Thus, the temperature regulator is needed at aqueous system for its stable electrochemistry and conductivity regulation of water (*e.g.* near freezing point). Non-aqueous solvents have virtue with these points of view.

The first suggestion of non-aqueous RFB is transition metal-ligand complex dissolved electrolyte by P. Singh at 1984. In this study, an acetonitrile-based electrolyte is suggested as non-aqueous supporting electrolytes. Firstly demonstrated non-aqueous RFB is ruthenium complex based system by T. Matsumura-inoue at 1988 [26]. This system expresses cell voltage of 2.6 V and this value is near twice higher than that of all-vanadium system (E_{cell} = 1.26 V). However, Wang *et al*. point out the flaw in the solubility of non-aqueous system (lower than 0.1 *M*) [7]. Compare to aqueous system,

a great scarcity of energy density from low solubility of redox couples is severe problem in non-aqueous based RFBs. To overcome this deficiency, several metal-ligand complexes and organic radicals are proposed as electrolyte for non-aqueous RFBs.

2.3.2.1 Metal-ligand complex based system

Stable redox reactions at several metal-ligand complexes are well-known phenomenon. Ferrocene is such example. Since ferrrocene/ferrocenium redox couple have high electrochemical and chemical stability by satisfaction of 18-electron rule, ferrocene is proposed as internal reference for non-aqueous electrolyte based electrochemical measurements by IUPAC [27]. From this reason, several research groups suggest those metal-ligand complexes as flow battery active materials [9, 10, 28]. Several ligands are regarded as compartment molecules for redox couples until now. Bipyridine, acetylacetonate and cyclopentadienyl ligands are such examples. Especially, vanadium acetylacetonate ($V(acac)_3$) based electrolyte is one of the most developed systems [10]. Proposed redox reaction mechanisms for $V(acac)_3$ by Monroe *et al.* are demonstrated as:

$$\text{Positive electrolyte: } V(IV)(acac)_3 + e \leftrightarrow V(III)(acac)_3 \quad E = 0.40 \text{ V } (vs.\ Ag/Ag^+)$$

$$\text{Negative electrolyte: } V(III)(acac)_3 + e \leftrightarrow V(II)(acac)_3 \quad E = -1.80 \text{ V } (vs.\ Ag/Ag^+)$$

Theoretical cell voltage is 2.2 V with this single redox couple and solubility at

acetonitrile solvent reaches 1.0 *M* at room temperature. Hence, the theoretical energy density of $V(acac)_3$ RFB is higher than aqueous RFB systems. However, further study reveals that practical solubility (solubility at electrolyte with more than 1.0 *M* of salt concentration) is less than 0.2 *M* [11]. This practical solubility is major drawback for $V(acac)_3$ system. Furthermore, the ligand substitution reaction is observed at acetylacetonate ligand [14]. It is because acetylacetonate is relatively weak-binding bidentate ligand. Therefore, chemical stability of $V(acac)_3$ is another problem for practical applications.

2.3.2.2 Organic molecule based system

In protic solvents such as water, organic radicals are not quite reversible and organic molecules are insoluble at polar solvents in general. Pinacol conversion of ketyl radical is typical example for chemical conversion of electrochemically generated free radical [29]. However, in aprotic organic solvents, several permanent free radicals with high solubility are observed. From potential cost-effectiveness of organic redox couples, the organic molecule-based RFB is widely suggested [12, 13, 30, 31]. Early system is 2,2,6,6-tetramethyl-1-piperidinyloxy (TEMPO) and *N*-methylphthalimide based RFB [12]. This cell yields cell voltage with 1.6 V and very stable cycleability is observed. Another prototype of all-organic RFB is suggested by Argonne national laboratory. This all-organic RFB comprises overcharge protection agents, 2,5-Di-*tert*-butyl-1,4-bis(2-methoxyethoxy)benzene as positive redox couple. The achieved cell voltage from two organic redox couples is near 1.6 V. However, the energy density of this cell only

reaches about 8.6 W h L^{-1} from the solubility limitation of positive redox couple [13]. Further suggested examples are Li/organic positive electrolyte-based cell. This type of cell employs negative electrode as Li metal and positive electrolyte as organic molecule dissolve supporting electrolyte solution [32]. Since the capacity of lithium metal is quite high, energy density of this cell solely depends on the energy density of positive electrolyte. TEMPO radical with Li salt dissolved carbonate supporting electrolyte is one of this examples [31]. The redox reaction of TEMPO/Li cell is suggested as:

$$\text{Positive electrolyte: } TEMPO^{+} + e \leftrightarrow TEMPO \quad E = 0.46 \text{ V (}vs\text{. NHE)}$$

$$\text{Negative electrode: } Li^{+} + e \leftrightarrow Li^{0} \quad E^{0} = -3.04 \text{ V (}vs\text{. SHE)}$$

Achieved energy density of TEMPO/Li cell is about 188 W h L^{-1} from 3.5 V of cell voltage and 2.0 *M* of active material concentration. However, dendritic growth of lithium metal and dead lithium formation are also problematic in these type of cell like lithium-ion batteries. Potential degradation mechanism of these organic radical-based RFB is the radical-supporting electrolyte compatibility [33]. Electrochemically generated organic radicals can chemically react with supporting electrolyte components. Therefore, fine-tuning of salt-solvent composition is essential for comprising organic molecules as RFB active species.

2.3.2.3 Semi-solid suspension based system

Lithium-ion battery (LIB) possesses the highest energy density in secondary batteries. To adopt this desirable characteristic, several studies focused on using active materials of LIB as RFB electrolyte solution [34]. The semi-solid suspension is composed of conductive carbon and active material dispersed lithium salt dissolved carbonate electrolyte solution. One of the early system comprises $LiCoO_2$ and $Li_4Ti_5O_{12}$ as positive and negative suspension component, respectively. The redox reaction is:

Positive suspension: $Li_{1-x}CoO_2 + xLi^+ + xe \leftrightarrow LiCoO_2 \quad E_{avg} = 4.00$ V (*vs*. Li/Li^+)

Negative suspension: $Li_4Ti_5O_{12} + 3e \leftrightarrow Li_7Ti_5O_{12} \quad E_{avg} = 1.55$ V (*vs*. Li/Li^+)

The continuous flowing cell demonstrates very limited performance with this slurry solution. To enhance this characteristic, redox mediator is applied as indirect electron transfer catalyst for active materials [35]. A solid, far from the inert electrode surface is indirectly charged or discharged by the redox mediator in supporting electrolyte. Hence, the redox potential tailoring of mediator in electrolyte is crucial in suspension-comprised system.

2.3.2.4 Polymer-dissolved electrolyte based system

Single-ion exchange membrane (both cation and anion) is one of the most expensive components in electrode stack. Furthermore, the cross-contamination of electrolyte gradually continues with degradation of separator. It is because the separator in RFB is

exposed at both very reductive and oxidative environments. To resolve this crucial issue, the polymer-dissolved electrolyte is suggested as flow battery electrolytes. The potential advantages of high molecular weight polymer solution is that simple dialysis membrane can be employed as separator [36, 37]. However, the potential degradation of polymeric components and relative low cell voltage are drawbacks for suggested systems. Furthermore, the viscosity of electrolyte solution should be improved to use as commercial RFB electrolytes [37]. Poly(boron-dipyrromethene) and polythiophene based RFB are examples for polymer-dissolved electrolyte solution [36, 38]. The *n*-doping and *p*-doping polymer are used as negative and positive electrolyte, respectively.

3. Experimental

3.1. Synthesis of Ni(II)-chelated complex cations

3.1.1 Synthesis of Ni(II)(azamacrocyclic ligands)X_2 (X = Cl^-, ClO_4^-)

Complex cations were synthesized by following literature [39]. The 1,4,8,11-tetraazacyclotetradecane (cyclam, Alfa Aesar, 98%) or 1,4,7,10-tetraazacyclododecane (Sigma Aldrich, 97%) or 1,4,8,12-Tetraazacyclopentadecane (Sigma Aldrich, 97%) was added into ethanol solution of nickel(II) chloride (Alfa Aesar, 98%) or Ni(II) perchlorate (Alfa Aesar, 98%). The molar ratio of metal-ion and macrocyclic ligand was unity. A precipitate was collected by filtration and dried under vacuum at 80 ℃, 12 h before use.

3.1.2 Synthesis of Ni(II)(cyclam)X_2 (X = Tf^-, $TFSI^-$)

Ni(II) complex cations with trifluoromethanesulfonate anion (triflate, Tf-) or bis(trifluoromethane)sulfonamide anion ($TFSI^-$) were synthesized by following literature [40]. Cyclam (Alfa Aesar, 98%) was added into anhydrous acetonitrile (AN, Alfa Aesar, anhydrous, 99.8+%) solution of nickel(II) triflate (Sigma Aldrich, 96%) or Ni(II)$[TFSI]_2$ (Sigma Aldrich, 95%). The molar ratio of metal-ion and macrocyclic ligand was unity. A precipitate was collected by centrifuge and dried under vacuum at 80 ℃, 12 h before use.

3.2. Electrochemical characterization

3.2.1 Cyclic voltammetry

Sample electrolyte for cyclic voltammetry was prepared by dissolving 10 m*M* redox couples into various supporting electrolytes. Both redox couple and salt for electrochemical characterization were dried under vacuum at 80 ℃, 12 h before use. Cyclic voltammetry test was conducted with glassy carbon working electrode (CHI 104, Area = 0.07 cm^2), silver wire quasi-reference electrode (Sigma Aldrich, 99.9% trace metals basis), and platinum flag counter electrode in argon filled glove box (Model HE-493/Mo-5, Vac. Co.). Cyclic voltammograms were recorded by CHI 660A electrochemical workstation at room temperature. After measuring cyclic voltammetry, ferrocene (Sigma Aldrich, 98%) was added to measured solution for correcting quasi-reference electrode. Note that the internal reference voltage of Fc/Fc^+ redox couple is equivalent with 0.40 V (*vs*. SHE) and 3.44 V (*vs*. Li/Li^+).

3.2.2 Cell preparation and galvanostatic cell cycling

3.2.2.1 Non-flowing H-cell test

Electrochemical characterization of redox couples was conducted by various types of cell at room temperature. Homemade H-cell was composed of two carbon papers (Toray, TGP-H-60) as inert electrode and tetraethylammonium cation (TEA^+) exchange exchange membrane (FuMA-Tech, Germany, fumapem®, F-14100). Cation exchange membrane was pre-soaked at least 12 h in various supporting electrolytes before

conducting non-flowing static cell test.

3.2.2.2 Non-flowing coin-cell test

Galvanostatic charge and discharge experiment was conducted by using modified 2032 coin-cell. Carbon paper (Toray, TGP-H-60) was used as inert electrode for electrochemical characterization. Carbon paper was pre-wetted with redox couples dissolved in supporting electrolyte, 12 h. Before the cycling, the cation-exchange membrane (FuMA-Tech, Germany, fumapem®, F-14100) was pre-soaked at least 12 h in the supporting electrolyte solution.

3.2.2.3 Flow battery test

Galvanostatic charge and discharge experiment was conducted by using homemade flow battery in nitrogen-purged chamber at Korea Electronics Technology Institute (KETI, collaborated with Professor Kim, Ki Jae). Carbon felt was used as inert electrode for electrochemical characterization. Before the cycling, the cation-exchange membrane (FuMA-Tech, Germany, fumapem®, F-14100) was pre-soaked at least 12 h in the supporting electrolyte solution.

3.2.3 Electrochemical quartz crystal microbalance (EQCM) test

Homemade EQCM cell was composed of platinum-coated quartz crystal electrode (Area = 0.196 cm^2), silver wire quasi-reference electrode and platinum flag counter electrode. Cyclic voltammetry test was collected by CHI 660A electrochemical work

station. The resonance frequency of quartz crystal electrode was recorded by SEIKO co. 922A. The increase/decrease of electrode mass were calculated by using Sauerbrey equation. Sauerbrey equation is described as:

$$\Delta f = -\frac{2f_0^2}{A\sqrt{\rho_q \mu_q}}\Delta m$$

where, Δf is frequency change, f_0 is resonance frequency, A stands for piezoelectrically active quartz crystal area, ρ_q is quartz density, μ_q is shear modulus of quartz and Δm is mass change of quartz electrode.

3.2.4 Galvanostatic intermittent titration technique (GITT)

GITT experiment was conducted at homemade H-cell. The state-of-charge (SOC) at electrode surface can be traced by quasi-open circuit voltage (QOCV) values. Current-applied and rest period were 10 min and 20 min, respectively. The closed-circuit voltage (CCV) was recorded at charging-ends and QOCV was obtained at rest-ends. The current and voltage points are recorded by WonA-Tech battery cycler (WBCS-3000).

3.3. Spectroscopic characterization

3.3.1 Surface analysis of inert electrode

To examine surface morphology and composition of used inert carbon electrode

surface, X-ray photoelectron spectroscopy (XPS; Sigma probe, Thermo) and field-emission scanning electron microscope (FE-SEM; JSM-6700F, JEOL) analysis were conducted. The X-ray source of XPS was Al Kα (1486.6 eV) and spot size of X-ray was 400 μm^2.

3.3.2 Assignment of metal-ligand complex

Synthesized nickel(II)-chelated azamacrocyclic ligand complexes were characterized by Fourier transform infrared spectroscopy (FT-IR). The pelletized powder was measured at vacuum atmosphere by using potassium bromide as IR window. The transmittance mode was used for measuring pelletized sample. FT-IR data was recorded by Nicolet 6700 (Thermo Scientific, USA).

3.3.3 Post-mortem electrolyte analysis

To analyze the redox states of redox couples, electron spin resonance spectroscopy (ESR) was recorded at various SOCs. The electrolyte was charged or discharged at homemade H-cell and the electrolyte was extracted for post-mortem analysis of electrolyte by ESR. ESR was recorded at – 150 ℃ by cooling liquid nitrogen.

3.3.4 Maximum solubility measurement

Excess amounts of transition metal-centered redox couples were dissolved into supporting electrolytes. After stirring electrolyte solution 30 min at room temperature (25 ℃), the undissolved residue was filtrated by syringe filter (Whatman, 25 mm, 1

μm). The filtrate was measured by performing inductively-coupled plasma atomic emission spectroscopy (ICP-AES; OPTIMA 4300DV; PerkinElmer, MA, USA) at 167-782 nm with argon plasma (6000 K).

The solubility of organic redox couples was examined by the transparency of electrolyte solution. The solubility of organic redox couples was defined after 30 min stirring of redox couple-dissolved supporting electrolytes.

3.4. Quantitative analysis on thermal properties of solids

Thermal properties of solid redox couples are compared with differential scanning calorimetry (DSC; TA Instrument, UK) results. DSC was used to define the melting points and heat of fusions of solid redox couples. The temperature ramp of DSC was 10 ℃ min^{-1}.

3.5. Estimation of redox couple stability by theoretical calculation

Density functional theory (DFT) calculations were performed with the Gaussian09 program at Dongguk university (collaborated with Professor Han, Young-Kyu) [41]. The geometry optimization and energy calculations used Becke's three-parameter exchange functional in combination with the Lee–Yang–Parr correlation functional (B3LYP) [42, 43] and the standard 6-31G** basis set.

4. Results and discussion

4.1. Uncompensated resistance and inert electrode surface

The electrochemical reversibility of redox couple can be traced by the peak potential shifts with scan rate increment in cyclic voltammetry. Nernstian, however, also demonstrates shifts of peak potential at non-ideal practical systems from *iR* loss of three-electrode cell. The equivalent circuits for three electrode cell are demonstrated at **Figure 4**a and b. The equivalent circuit clearly demonstrates that the e_{true} (*vs*. reference electrode) is very dependent with uncompensated resistance (R_u). Since the Faradaic current increases at higher scan rates, the iR_u value is being higher with faster scan rate. Hence, two factors are must be separated to analyze electrochemistry of redox couples.

To examine electrochemical reversibility, therefore, the quantification of uncompensated resistance is inevitable. The equivalent circuit for three electrode cell at non-Faradaic region is shown at Figure 4b. The uncompensated resistance of three-electrode cell at non-Faradaic region can be calculated by:

$$i = \frac{E}{R_u} e^{-t/R_u C_{dl}}$$

where, i is flowed current, E is applied potential, t is time and C_{dl} is double-layer capacitance of working electrode. Thus, the R_u can be calculated from the current at starting point of potential applied. Fig. 4c is the chronoamperogram from 0.5 V (*vs*. Ag wire) applied used three electrode cell. Note that voltage step is at non-Faradaic region.

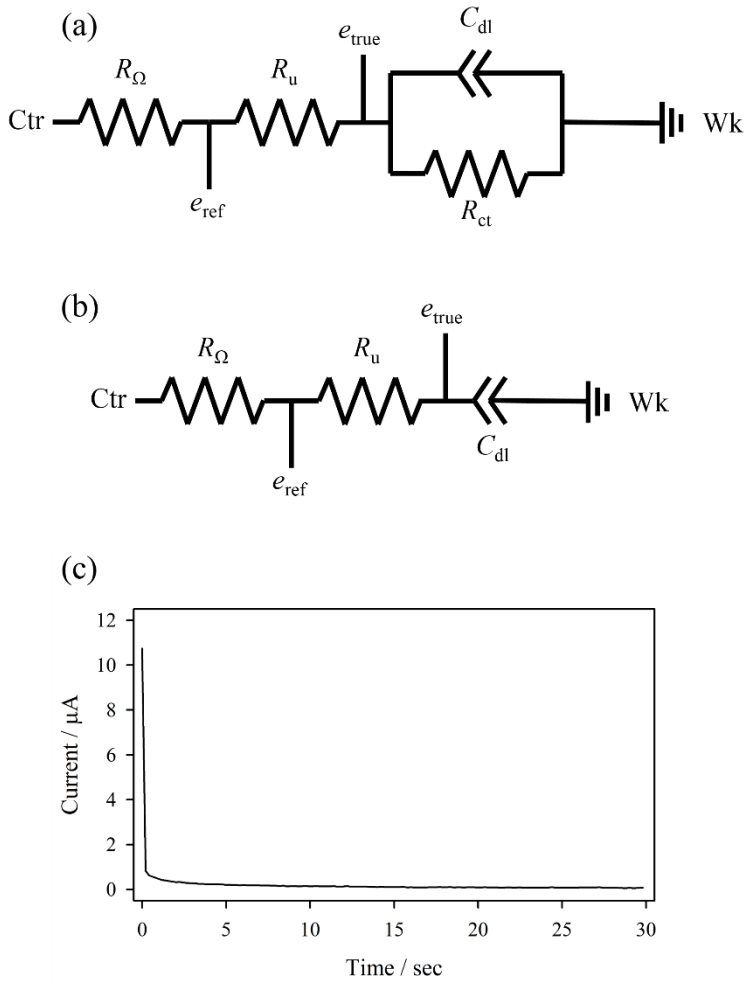

Fig. 4 Equivalent circuits of: (a); three-electrode cell at charge transfer region (b); at non-Faradaic region. (c); chronoamperogram of used three electrode cell at voltage step of 0.5 V (*vs*. Ag wire)

Calculated R_u is 60.4 Ω at 1.0 *M* tetraethylammonium tetrafluoroborate ($TEABF_4$) dissolved propylene carbonate (PC) supporting electrolyte, room temperature. Since *iR* drop voltage from R_u is 5 mV at 10^{-5} A of current scale (typical current value from 10 m*M* of redox couple dissolved supporting electrolyte at 300 mV s^{-1} of scan rate), the shift of peak potential higher than 5 mV at scan rate of 300 mV s^{-1} is the response from the electrochemical kinetics of redox couples. Thus, the scan-rate-dependent voltammogram can be used for interpreting electrochemical kinetics in homemade three electrode cell.

Since electrochemical reaction only takes place at the surface of the inert electrode, the surface composition of electrode should be addressed before analysis. FE-SEM and XPS can be a reliable tools for analyzing morphology and chemical composition of electrode surface. Carbon paper is used as inert electrode at the galvanostatic charge-discharge experiments. Chemical composition and surface morphology of inert electrode are demonstrated at **Figure 5**. The carbon 1s (C 1s) XPS spectra were fitted with binding energy values indicated at **Table 1** [44, 45]. FE-SEM image reveals that the surface of carbon paper electrode is very smooth without voids. The pores of carbon paper electrode is in the range of 20 to 30 μm, which is enough cavity for containing electrolyte solution for galvanostatic cycling. The chemical composition of electrode is crucial for electrochemistry. The surface of carbon paper inert electrode is very hydrophobic from its hydrocarbon-dominated chemical composition. Therefore, the adsorption on electrode surface during redox reaction of polar redox-active molecule is doubtful because the polar/non-polar interaction is not favorable, generally.

Table. 1 Assigned peaks for C 1s X-ray photoelectron spectra (XPS) of graphitic carbon electrode [44, 45]

C 1s	Binding Energy / eV
C-C, -CH_2	285.0
C-O	286.5
O-C-O, C=O	287.6

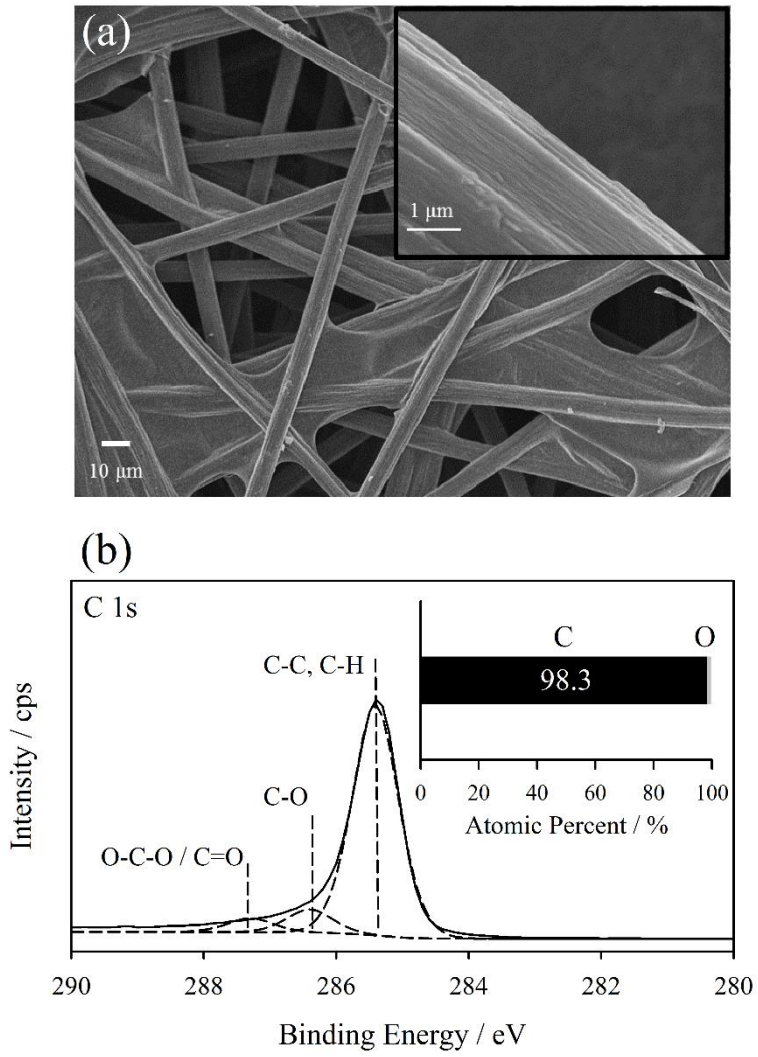

Fig. 5 (a); FE-SEM image of used carbon paper electrode and magnified surface image of carbon paper (inset) (b); C 1s XPS spectra obtained from carbon paper inert electrode. Inset: atomic composition of inert electrode surface, which was calculated from the XPS data.

4.2. Verification of thermodynamic parameters for solubility enhancement of redox couples

The solubility prediction equation for ideal solution indicates that the low heat of fusion and melting point is desirable for higher solubility of solute molecules. To verify this rule-of-thumb, the model system is designed. The benzoquinone (BQ) molecule is used for model system. BQ is highly symmetric molecule and well-known for redox-active molecule [46]. To reduce the melting point of pristine BQ, the asymmetric aliphatic chain is introduced. In other words, the empirical rule, Carnelley's rule is applied at BQ molecules. Carnelley's rule states that the highly symmetrical molecule has the high melting points [15]. Therefore, more bulky functional group is introduced on pristine BQ, lower melting point is expected and thereby the solubility should be increased. *tert*-Butyl (t-BQ) and methyl (m-BQ) groups are selected for increasing asymmetric degree of pristine molecules.

Figure 6 demonstrates molecular structures of BQ derivatives and its thermal and physicochemical properties. Figure 6a shows molecular structures of BQ derivatives. With introduction of bulky functional groups, the decrease of melting point is observed. Figure 6b illustrates that the thermal properties of BQ derivatives measured by DSC. The DSC results reveal that the melting point of BQ is greatly reduced and the value is about 40 ℃ at m-BQ. This result is well-correlated with the Carnelley's rule aforementioned. Moreover, as we expected at solubility equation, increase of solubility

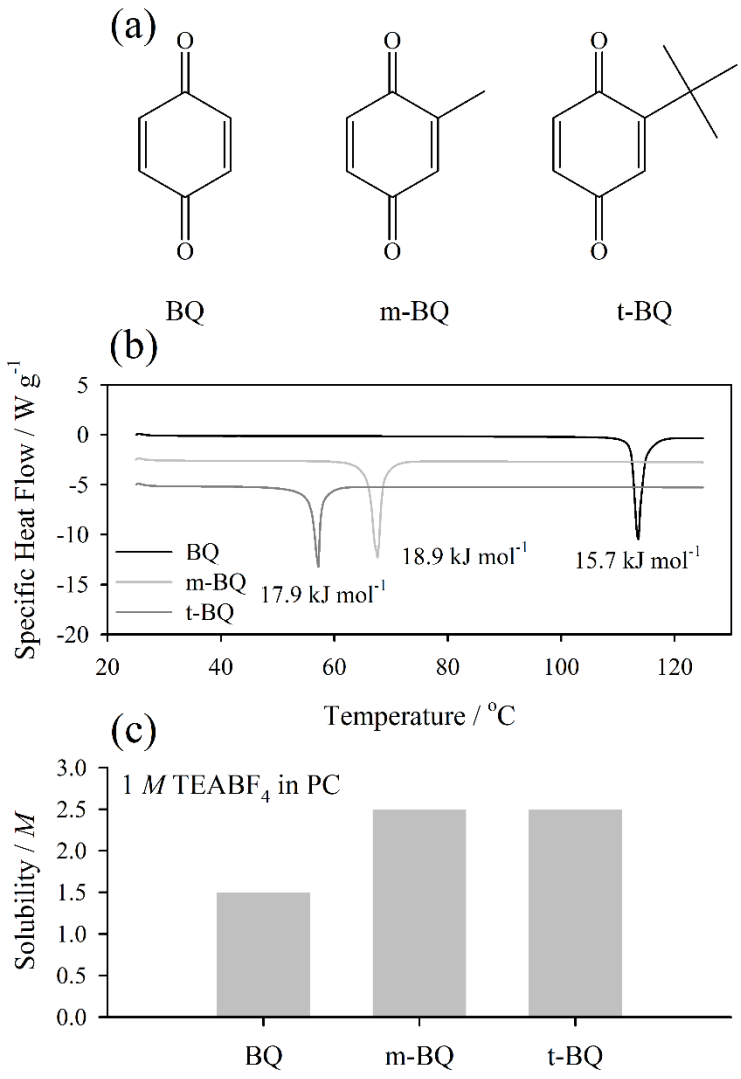

Fig. 6 (a); Three derivatives of benzoquinone (BQ). (b); Differential scanning calorimetry (DSC) results of BQ derivatives and (c); measured solubility at 1.0 *M* $TEABF_4$ in PC supporting electrolyte

is observed at both methyl and *tert*-butyl introduced molecules. Two molecules possess 1.67 times higher solubility (2.5 *M*) than BQ molecule (1.5 *M*) at PC-based supporting electrolyte. Reasoning from cause to effect, we deduce that the given equation can be applied to improve redox couples for non-aqueous RFBs.

4.3. A tetradentate azamacrocylic Ni(II) complex cation as a single redox couple for non-aqueous flow batteries

Since metal-ligand complexes can demonstrate multiple oxidation states by electrochemical redox reactions of center metal-ions, the application of metal-ligand complexes as redox couple for RFB system can be possible. A tetradentate ligand molecule has further advantages as ligand candidates. Firstly, the multiple oxidation states from single metal-ion center can be possible with strong chelation chemistry of multidentate ligand. Thus, a single redox can be designed by comprising multidentate ligand molecule. A single redox couple has advantageous features as flow battery electrolyte. In dual electrolyte, the cross-contamination should be occurred by concentration gradient across separator. It is because the concentrations of redox couple at each electrolyte solution are disparate negative or positive redox couples. Hence, the permanent loss of redox couples is resulted. The permanent loss of redox couple makes several deficiencies: *i*) distortion of N/P ratio, *ii*) capacity degradation from active material loss, *iii*) degradation of Coulombic efficiency, *iv*) additional cost for separating contaminated redox couples. However, the single redox couple can

eliminate several problematic features from dual-electrolyte used RFBs. In single electrolyte, the same species are dissolved in the electrolyte at discharged state. After charging of battery, the reduced and oxidized form of redox couple are generated in electrode stack. Therefore, the cross-contamination of redox couple is also occurred in single electrolyte utilized RFBs and resulted in self-discharge of redox couples. A single redox couple, however, has the identical discharged state at both positive and negative electrolyte. Thus, there is only degradation of Coulombic efficiency of cell in single redox couple comprised cell because the discharged species in both electrolytes are unity. The longer service life is expected by single redox couple and it is desirable feature for large scale ESSs.

4.3.1 The effects of cavity size and counter anion on the electrochemistry and solubility of complex cation

An azamacrocyclic complex cation dissolved solution is composed of ligand molecule, center metal-ion, counter anions and solvent molecules. Single redox couple for RFB system can be validated with tailoring of these four variables. Metal-ion center should be rather economical (not rare metals) and have redox potential within electrochemical stability window of supporting electrolyte (*i.e.* PC, 1.0 ~ 4.3 V *vs*. Li/Li^+, equivalent to -2.0 ~ 1.3 V *vs*. SHE). The brief value of redox potential can be decided by the Latimer diagram. **Figure 7** demonstrates the Latimer diagram at 1 *M* acid condition for several metal-ions. Figure 7 clearly indicates that the nickel(II) is proper metal-ion from its redox potentials and cost-effectiveness than other metal-ion candidates. Iron(II)

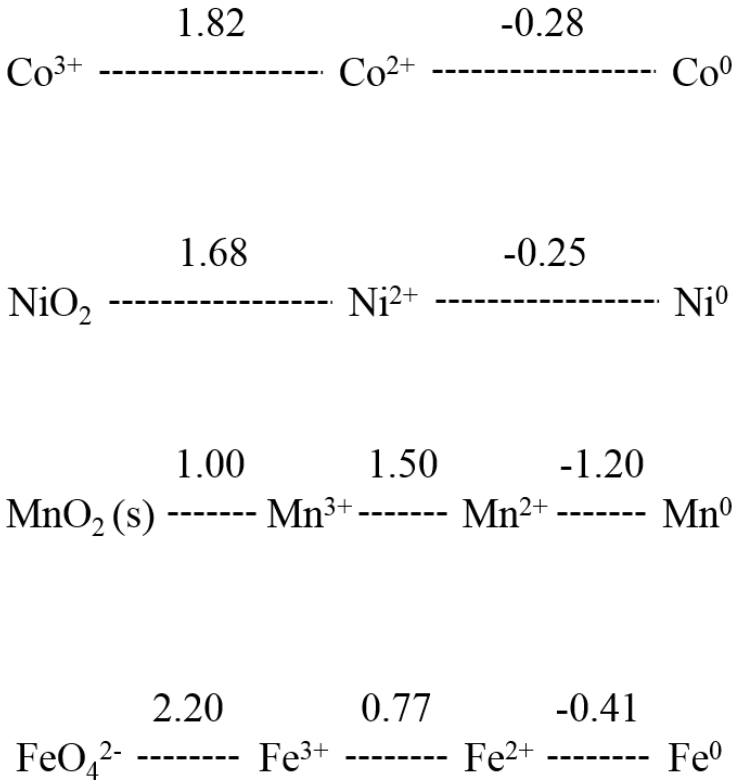

Fig. 7 Latimer diagrams of cobalt, nickel, manganese and iron at 1.0 *M* acidic condition. All potentials are demonstrated with *vs*. SHE.

also demonstrates redox potentials within electrochemical stability window of PC-based supporting electrolytes, however, has too low expected working voltage (1.18 V), which is lower than the aqueous RFBs (1.23 V).

Metal-ion undergoes change of ionic radius from its electrochemical redox reactions. Azamacrocyclic complex has best-fit metal-nitrogen (M-N) bond length for each metal-ions. For instance, Ni(II) has the value for M-N, 189 pm [47]. Hence, the cavity size of macrocyclic complex is crucial for chemically reversible redox reactions because the M-N value alters with the ionic radius changes. **Table 2** indicates the structures and best-fit M-N distances of general three azamacrocyclic ligands. The M-N distance is directly correlated with the ring size of azamacrocyclic ligands. Therefore, the ligand molecules have the compatibility with redox reactions of Ni(II) center. The smallest 1,4,7,10-Tetraazacyclododecane (cyclen, [12]aneN_4) could be a suitable ligand for Ni(II) to Ni(III) redox reaction and the largest 1,4,8,12-Tetraazacyclopentadecane ([15]aneN_4) might be fit for Ni(II) to Ni(I) redox reaction. A simple cyclic voltammetric response can define electrochemistry of Ni(II)-chelated azamacrocyclic complexes. **Figure 8** presents cyclic voltammograms from Ni(II)[12]aneN_4 dissolved supporting electrolytes. The oxidation of Ni(II) to Ni(III) is very stable at the half-wave potential of 0.96 V (*vs*. Fc/Fc^+). This result is well correlated with M-N distance change with electrochemical redox reaction. However, in the range of negative voltage, the Ni(II) to Ni(I) is chemically unstable because the enlarged M-N in Ni(I)-N is not stabilized in cyclen cyclic ligand. If Ni(I) is unstable in cyclen ligand, plating of Ni(II) is observed at negative voltage region. Figure 8b clearly presents reverse current

Table. 2 Nomenclature and abbreviation of azamacrocyclic ligand molecules and the best-fit metal-nitrogen bond distances for each ligand molecules

Nomenclature (abbreviation)	Molecular Structure	Best-fit M-N Distance / pm
1,4,7,10-Tetraazacyclododecane (cyclen, [12]aneN_4)	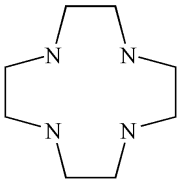	182
1,4,8,11-Tetraazacyclotetradecane (cyclam, [14]aneN_4)	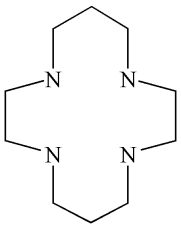	207
1,4,8,12-Tetraazacyclopentadecane ([15]aneN_4)	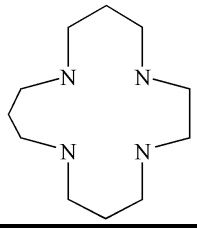	215

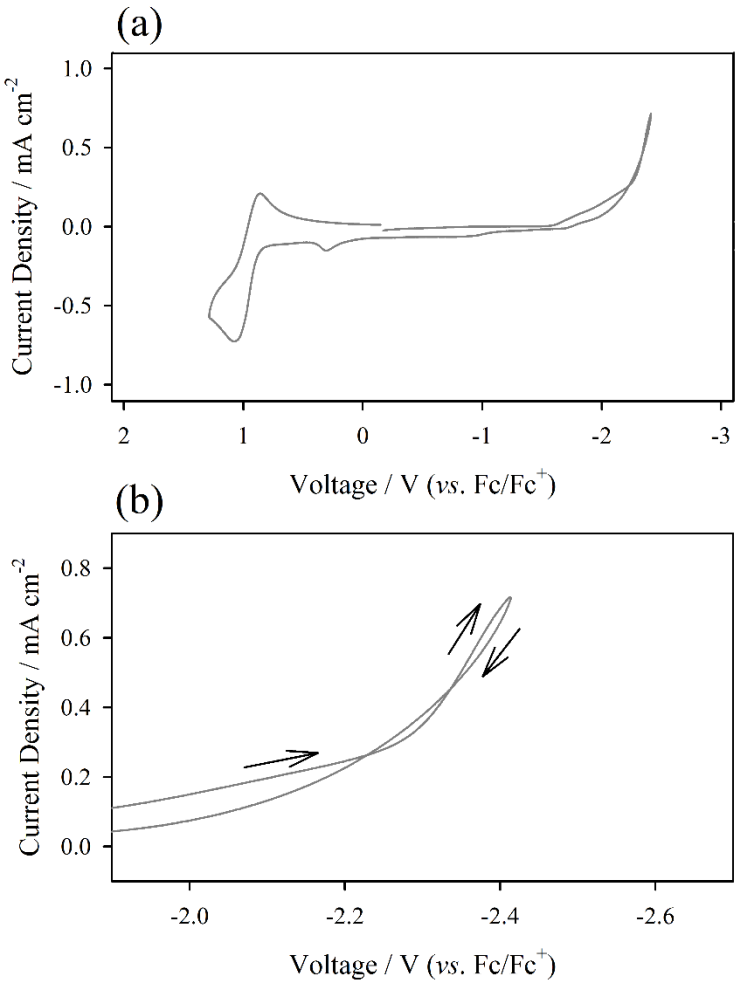

Fig. 8 (a); Cyclic voltammogram of 10 m*M* Ni(II)([12]aneN$_4$)[ClO$_4$]$_2$ complex dissolved 1.0 *M* TEABF$_4$ in PC supporting electrolyte and (b); magnified voltammogram at the reductive potential region. Scan rate = 100 mV s^{-1}

behavior at -2.0 to -2.4 V (*vs*. Fc/Fc^{+}) voltage region. This reverse current response is well-known at metal plating experiments. Thus, the unstable complex is dissociated at negative potential, which results in plating of Ni(II) at reductive potential region.

The enlarged cyclic ligand, 1,4,8,12-Tetraazacyclopentadecane ([15]aneN_4) also examined as a single redox couple. **Figure 9** shows the voltammogram from Ni(II)[15]aneN_4 dissolved supporting electrolyte. While the cyclen complex demonstrates irreversible redox reaction at reductive potential region, Ni(II)[15]aneN_4 is unstable at oxidative potential region. Latimer diagram suggests one possible region for this result. In the positive potential region, Ni(II) can be oxidized as insoluble oxide form (*i.e.* NiO_x). Therefore, the reduction of oxidized species is impossible at reverse sweep at Ni(II)[15]aneN_4 complex cation. Nonetheless, the reduction of Ni(II) to Ni(I) is quite stable in this complex. In summary, both the smallest and largest ligand molecules cannot demonstrate electrochemistry as a single redox couple. Hence, the concluded proper ligand size for a Ni(II)-chelated single redox couple is 1,4,8,11-tetraazacyclotetradecane ([14]aneN_4, cyclam).

Since azamacrocyclic ligand cannot donate electron in metal-ligand complex, the counter anion must be included in metal-ligand complex. Thus, counter anion is crucial to design redox couple because the electrochemistry and solubility of redox couple can be differed with the binding property of counter anions. Counter anions are classified as strongly binding or non-coordinating anion [48]. The solubility and electrochemical performances from two anions are defined by two cases. Rather strong Lewis base, chlorine anion (Cl^{-}) is selected as former and weak Lewis base, perchlorate

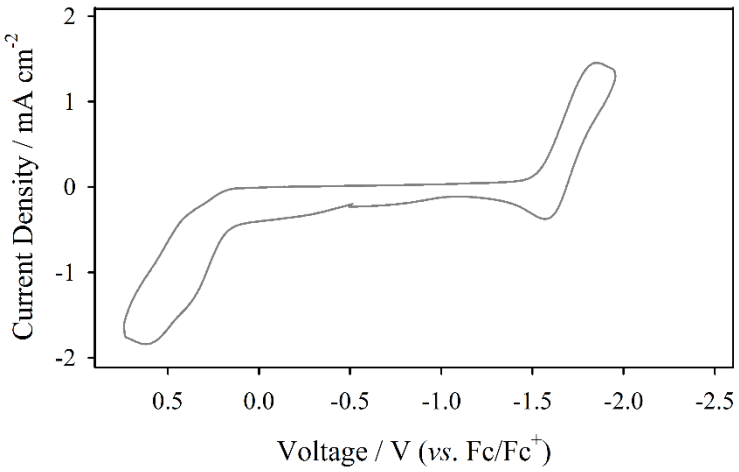

Fig. 9 Cyclic voltammogram of 10 m*M* Ni(II)([15]aneN$_4$)[ClO$_4$]$_2$ complex dissolved 1.0 *M* TEABF$_4$ in PC supporting electrolyte. Scan rate = 300 mV s^{-1}

anion (ClO_4^-) is comprised as latter case. From binding strength of two anions, the geometrical symmetry of two complexes are different as elongated octahedron for Cl^- and square planar for ClO_4^-. The concluded orbital structures from two complexes, therefore, are differed by group theory.

The obtained FT-IR spectra from precursors and synthesized complexes are demonstrate at **Figure 10**. Figure 10a presents spectra from precursors and final product. The synthesized product shows very distinct peaks at the wavenumber range of 800 to 1000 cm^{-1}. Figure 10b shows comparative FT-IR spectra of Ni(II)(cyclam) with Cl^- and ClO_4^-. Spectra from complexes clearly demonstrate the Ni-N bonding (800 to 1000 cm^{-1}) from complex cation and C-H bending vibration (1450 cm^{-1}) from ligand molecule as indicated Figure 10a. Difference between two complex cations is at the wavenumber range of 1000 to 1200 cm^{-1}. While signal from Ni(II)(cyclam)$[ClO_4]_2$ shows a broad peak from coordinating ClO_4 (about 1000 cm^{-1}) [49], there is no broad peak at the same region with Cl^-. Thus, the synthesized samples were characterized from the FT-IR spectra.

The molecular orbitals of two metal-ligand complexes and voltammetric response are illustrated at **Figure 11**. Figure 11a presents two orbital structures from two different complexes. While complex cation with Cl^- counter anions has the elongated octahedron geometry, with ClO_4^- belongs to the square planar geometry. It is because the properties of anions are very different, aforementioned. Two features are expected from the orbital structure and binding properties of anions. The cell voltage and solubility

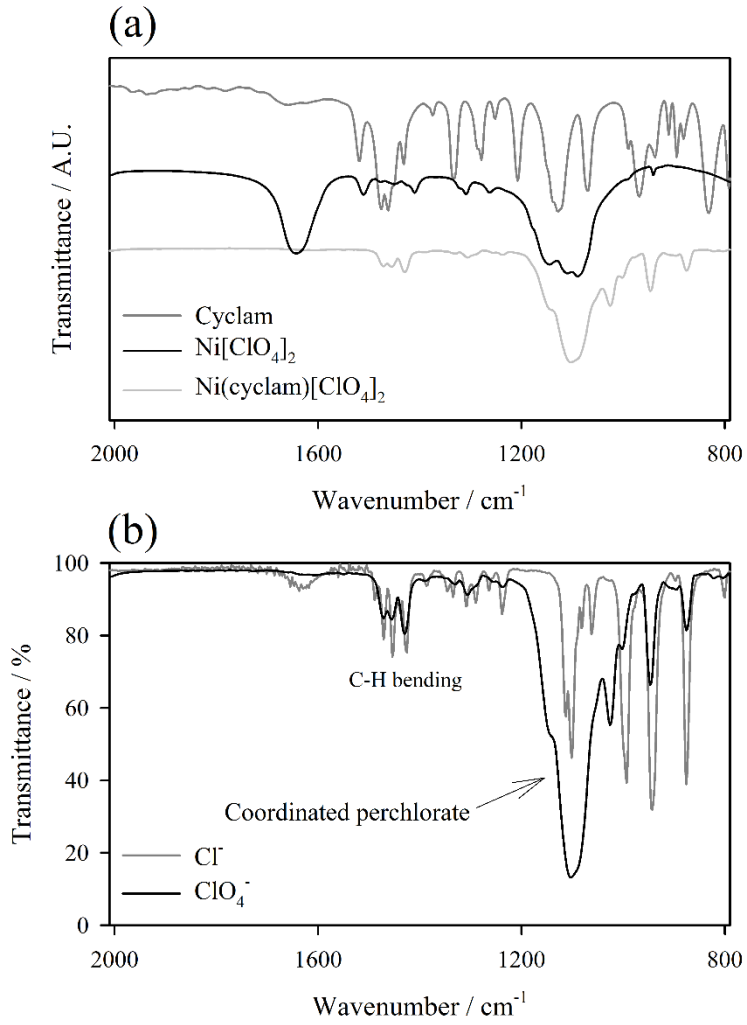

Fig. 10 FT-IR spectra of KBr-pelletized (a); cyclam, nickel(II) percholate and Ni(II)(cyclam)$[ClO_4]_2$ and (b); Ni(II)(cyclam)X_2 ($X = Cl^-, ClO_4^-$).

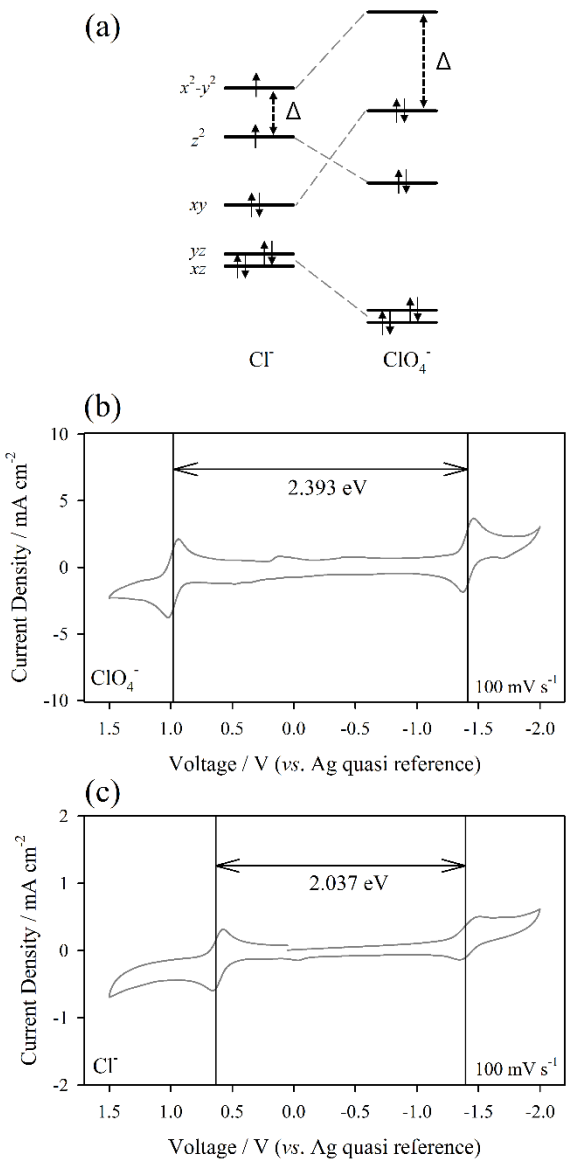

Fig. 11 (a); Orbital structure of Ni(II)(cyclam)Cl_2 and Ni(II)(cyclam)$[ClO_4]_2$. Cyclic voltammograms obtained from (b); 1 m*M* Ni(II)(cyclam)Cl_2 and (c); 10 m*M* Ni(II)(cyclam)$[ClO_4]_2$ dissolved 1.0 *M* $TEABF_4$ in AN supporting electrolyte. Scan rate = 100 mV s^{-1}

are those two performances. Firstly, the cell voltage should be different in two complexes. Cell voltage is defined as the potential difference between positive and negative electrolytes. In single electrolyte system, the potential difference is originated from the energy gap (Δ) between highest occupied molecular orbital (HOMO) and lowest un-occupied molecular orbital (LUMO) levels. The gap is also presented at Figure 11a. Since the energy level difference is higher at with ClO_4^- than Cl^-, the cell voltage should be higher at ClO_4^--attached complex. To examine cell voltage of two complexes, the cyclic voltammograms were recorded at both electrolytes. Figure 11b and 11c are voltammetric responses from complex cation with ClO_4^- and Cl^-, respectively. Cell voltage of two electrolyte is calculated by subtracting two half-wave potentials ($E_{1/2}$) of Ni(II) to Ni(III) and Ni(II) to Ni(I) redox reactions. Half-wave potential is mathematically defined as:

$$E_{1/2} = \frac{E_{p1} + E_{p2}}{2} = E^{0'} + \frac{RT}{nF} \ln \left(\frac{D_1}{D_2} \right)^{\frac{1}{2}}$$

where, E_{p1} and E_{p2} are the peak potential of forward electrochemical reaction and vice versa at certain temperature, respectively, R is gas constant, T is temperature, n is the number of equivalents of electron transferred, F is Faradaic constant and D_n is diffusion coefficients of pristine (1) and after redox reaction (2). Note that $E^{0'}$ is formal redox potential. Therefore, we can determine the formal redox potential from

half-wave potential at cyclic voltammetry experiment because the diffusion coefficient is nearly same at reduced or oxidized complexes with pristine complex. Calculated cell voltage is 2.393 V at ClO_4^- and 2.037 V at Cl^- anion. Cell voltages are altered by initial orbital state of complex cation, as a result.

Secondly, solubility is compared at two complexes. Dissolving process of ionic solid can be classified as two types; ion-pair and dissociation of cation and anion. It is expected that the solution with ion-pair is from Cl^- and dissociation is from ClO_4^- attached complex cation. The measured solubility at 1.0 *M* $TEABF_4$ in AN supporting electrolyte is 1 m*M* at Cl^- and 25 m*M* at ClO_4^- case. The 25-fold higher solubility is observed at non-coordinating anion case. In summary, non-coordinating anion (ClO_4^-) surpasses both cell voltage and solubility than strongly-coordinating anion (Cl^-). Since a solvent with high dielectric constant can dissolve ionic solid, the carbonate-based supporting electrolyte is introduced [4]. **Table 3** presents the dielectric constant of various supporting electrolytes and solubility of Ni(II)(cyclam)$[ClO_4]_2$ at supporting electrolytes, respectively. While AN has the lowest dielectric constant, the ethylene carbonate (EC) demonstrates the highest dielectric constant. However, EC cannot be used solely because EC is solid-state at room temperature. The EC/PC (1:1 = *v*/*v*) mixture, therefore, is used for high dielectric solvent. The maximum solubility reaches 400 m*M* at 1.0 *M* $TEABF_4$ in EC/PC supporting electrolytes. Note that this demonstrated solubility is four-fold higher than the threshold value (100 m*M*) from the previous reference [7]. Therefore, the promising single redox couple with sufficient physicochemical properties for non-aqueous flow batteries is designed by ClO_4^- anion.

Table. 3 Dielectric constants of various solvents [4, 50] and solubility of Ni(II)(cyclam)$[ClO_4]_2$ at 1.0 *M* $TEABF_4$ dissolved supporting electrolytes

Solvents	Dielectric constants	Solubility / m*M*
Acetonitrile	36.6	25
Propylene carbonate (PC, 25 ℃)	64.9	300
Propylene carbonate (40 ℃)	61.7	-
Ethylene carbonate (EC, 40 ℃)	89.1	-
EC/PC (1:1 = *v*/*v*), 25 ℃	-	400

4.3.2 The electrochemistry of Ni(II)(cyclam)$[ClO_4]_2$ and its application for non-aqueous flow battery electrolyte

The electrochemistry of complex cation is examined as a single redox couple for non-aqueous RFB. Since the redox couple is applied as flow battery active material, the potential difference, chemical stability, charge transfer kinetics and diffusion rate are at least necessities. Four features are handled by the electrochemical response from cyclic voltammetry-based experiment.

The scan-rate-dependent cyclic voltammograms are recorded for cyclam complex. **Figure 12** presents the voltammograms recorded at positive and negative voltage region, respectively. Figure 12a shows the molecular structure of Ni(II)(cyclam). The strong tetradentate structure is observed at cyclam complex. Peak potentials from positive redox reaction at positive and negative sweep are 0.85 and 0.62 V (*vs*. Fc/Fc^+), respectively at 300 mV s^{-1} (Figure 12b). Thus, the redox potential from positive redox couple is 0.74 V (vs. Fc/Fc^+). At the negative potential sweep, the peak potentials at 300 mV s^{-1} of Ni(II) to Ni(I) is observed at -1.90 V and vice versa is at -1.71 V (*vs*. Fc/Fc^+) (Figure 12c). Redox potential of negative redox couple is -1.81 V (*vs*. Fc/Fc^+). Note that the peak currents ratio is near unity ($i_{pc}/i_{pa} \approx 1$) for both oxidation and reduction. The expected cell voltage from the redox couple is 2.55 V, which is twice higher value than theoretically fully-utilized cell voltage from aqueous electrolytes (1.23 V). Electrochemical kinetics of Ni(II)(cyclam) complex cation is examined by comparing heterogeneous rate constants (k_s) with all-vanadium RFB (VRFB). The charge transfer rate of redox couple can be compared by considering the values of k_s at

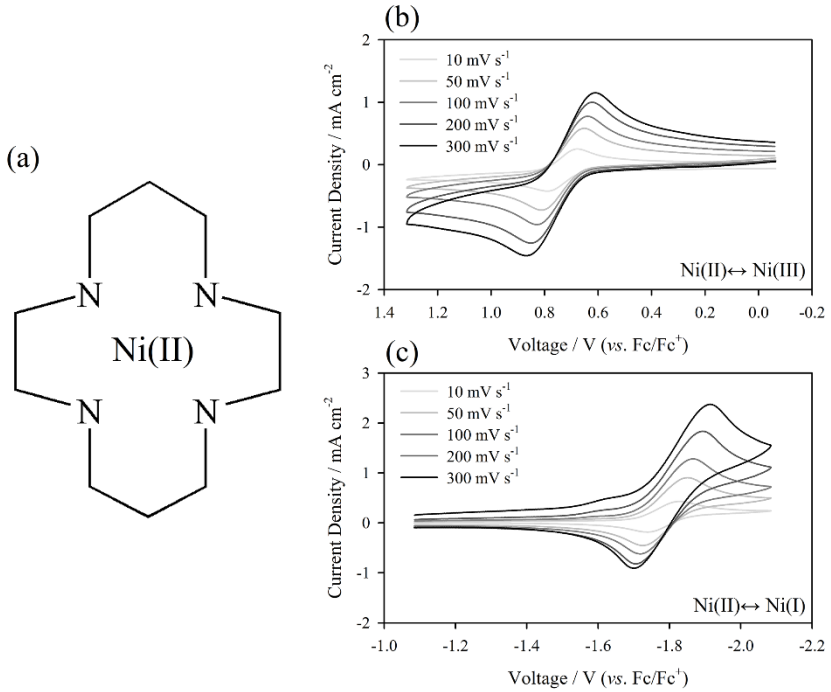

Fig. 12 (a); Molecular structure of Ni(II)(cyclam) and cyclic voltammograms from 10 m*M* Ni(II)(cyclam) dissolved 0.5 *M* $TEABF_4$ in EC/PC electrolyte for (b); Ni(II) to Ni(III) and (c); Ni(II) to Ni(I) redox reaction. Scan rates are indicated in the inset.

same inert electrode. At carbon surface, the k_s of VRFB is 1.71×10^{-5} cm s^{-1} from result of M. Skyllas-Kazacos [18]. The peak current (i_p) is expressed as the function of $E_p - E^{0'}$(polarization). The equation is [51]:

$$i_p = 0.227FAC_O^* k_s e^{\left[-\frac{\alpha nF}{RT}\left(E_p - E^{0'}\right)\right]}$$

Since the k_s value can be calculated from the intercept of natural logarithm of i_p *vs*. polarization, the plot is indicated at **Figure 13**. The additional N/P ratio modification from kinetic difference in electrode stack is not necessary because the charge transfer kinetics of two electrolyte is nearly identical. Furthermore, the electrode kinetics of both oxidation and reduction reactions are more facile than that value of VRFB demonstrated. Thus, the energy loss from polarization can be greatly suppressed in Ni(II)cyclam comprised RFBs.

To define the chemical stability of complex cation, cyclic voltammogram is recorded, repeatedly. Figure 14a presents the electrochemical stability window of supporting electrolyte and redox reaction of Ni(II)(cyclam). The redox reaction takes place within electrochemical stability window. Hence, the electrolyte decomposition does not exist in Ni(II)(cyclam)-comprised cells. The electrolyte solution after voltammetry, the residues of reduced and oxidized species of Ni(II)(cyclam) are remained because the redox couples after voltage sweep are diffuse-out from the electrode surface. If there are chemical reaction or degradation of residues in electrolyte solution, the new peak currents or distortion of currents will be observed in voltammogram. Nevertheless, the

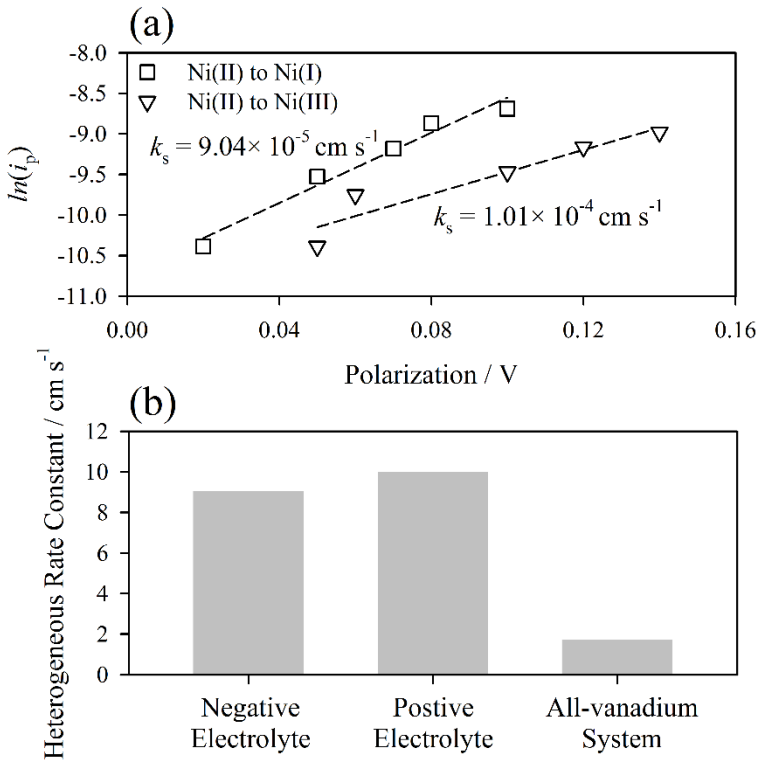

Fig. 13 (a); ln(i_p) *vs*. polarization plots and (b); calculated heterogeneous rate constants of Ni(II)(cyclam) and all-vanadium system

Ni(II)cyclam demonstrates well overlapped voltammogram with two, 1st cycle and 50th cycle. Hence, the chemical stability and electrochemical reversibility of Ni(II) chelated cyclam is established by this result. Further examination of chemical stability is conducted with EQCM test. As aforementioned, expected side reactions from Ni(II) complex cation and organic electrolyte are Ni plating, oxide formation and film formation by electrolyte decomposition. Since all of expected side reactions resulted in mass increase of inert electrode, the EQCM is effective approach for estimating chemical stability of Ni(II)(cyclam). **Figure 15** demonstrates the sweep segments from voltammogram on EQCM surface and mass change of inert electrode during repeated electrochemical reactions. As indicated at Figure 15b, no mass increment of inert electrode is observed. It is because there are no side reactions from electrolyte components. The stable cycleability, therefore, is expected from Ni(II)(cyclam) comprised cells.

The diffusion rate of redox couples dissolved in concentrated electrolyte is crucial for rate capability of RFB because the charge transfer reaction occurs at Nernst diffusion layer (near electrode surface), which is the diffusion-controlled region. The diffusion coefficient of Ni(II)(cyclam) is calculated by Randles-Sevcik equation. Randles-Sevcik equation is [51]:

$$i_p = (2.99 \times 10^5) n^{3/2} \alpha^{1/2} A D^{1/2} C \nu^{1/2}$$

$$|E_p - E_{p/2}| = 47.7 / \alpha \text{ mV at } 25℃$$

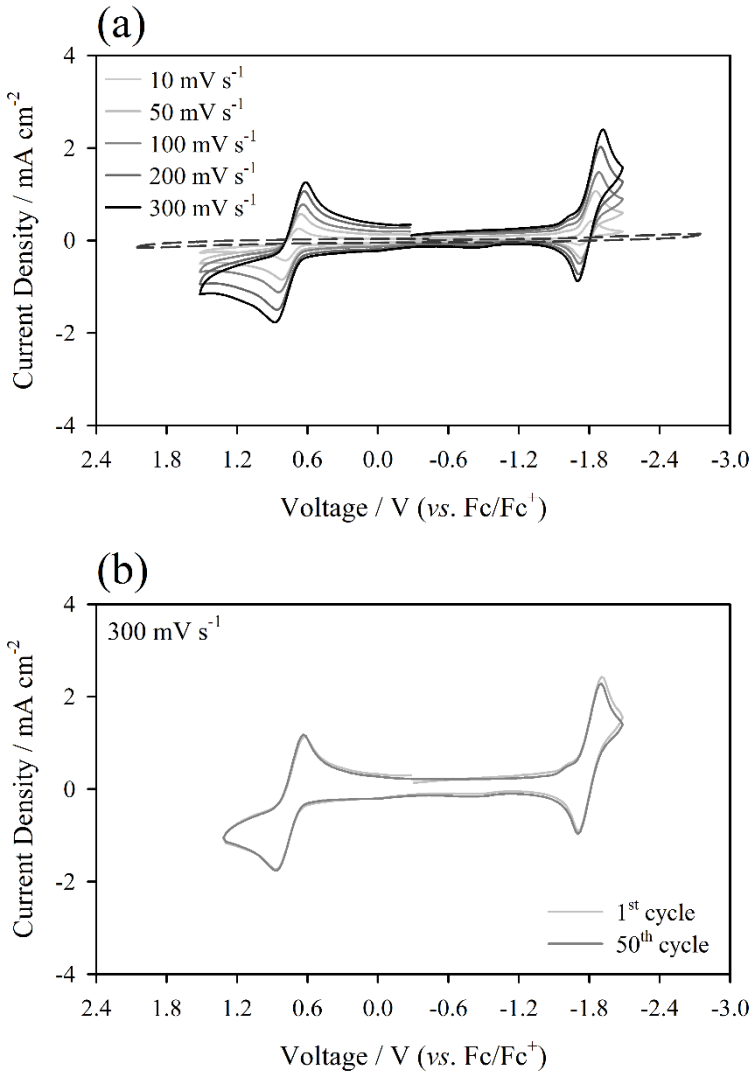

Fig. 14 (a); Scan-rate-dependent cyclic voltammograms with electrochemical stability window of supporting electrolyte and (b); 1st and 50th repeated voltammograms of Ni(II)(cyclam). Scan rate for supporting electrolyte = 10 mV s^{-1}.

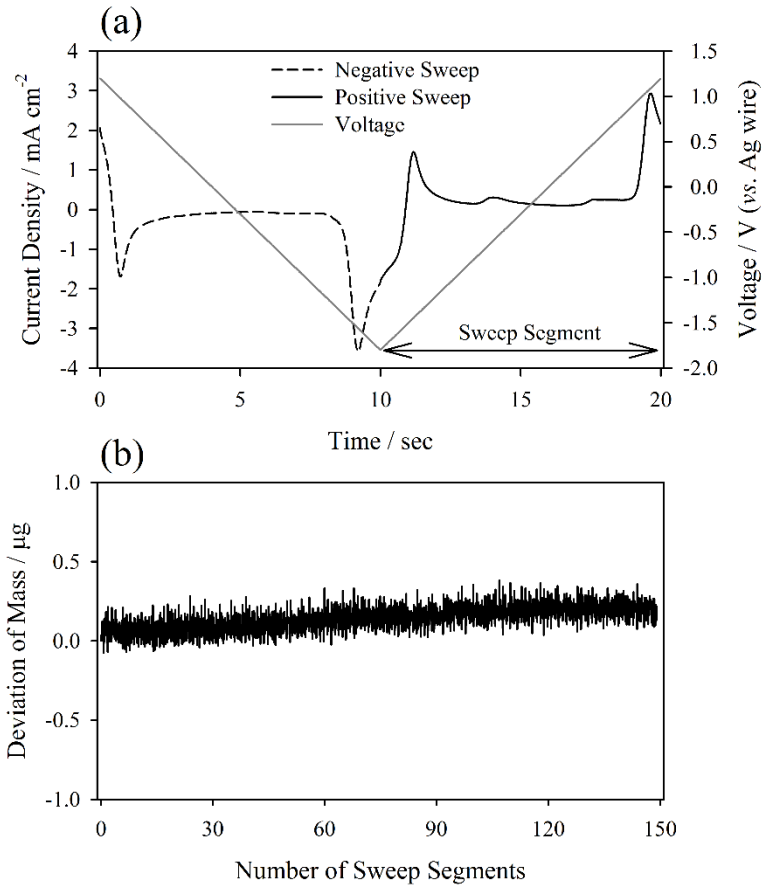

Fig. 15 (a); Sweep segments from cyclic voltammetry on platinum-coated quartz crystal electrode surface and (b); mass change of inert electrode traced by EQCM at Ni(II)(cyclam) dissolved electrolyte. Scan rate = 300 mV s^{-1}

where, i_p is peak current value, n is the number of electron transferred, α is charge transfer coefficient calculated from the difference of peak potential (E_p) and half-peak potential ($E_{p/2}$), A is used inert electrode area, D is diffusion coefficient, C is concentration of redox couple and v stands for scan rate of recorded voltammogram. **Figure 16** demonstrates the voltammograms at 0.4 *M* of Ni(II)(cyclam) dissolved 0.5 *M* $TEABF_4$ in EC/PC (1:1 = *v*/*v*) and Randles-Sevcik plot from the Figure 15a and 15b. The range of diffusion coefficient is in the 10^{-6} to 10^{-7} cm^2 s^{-1} order-of-magnitude and these values are quite high at non-aqueous electrolyte [10, 52].

Galvanostatic charge-discharge experiment is conducted at home made H-cell. **Figure 17** presents exploded view of H-cell. Two carbon paper electrodes are soaked in each electrolyte reservoirs, respectively before cycling. **Figure 18** shows the accumulated capacity *vs*. voltage curves of 10 m*M* Ni(II)(cyclam) electrolyte and cycleability at H-cell. The charging voltage plateau is observed near 2.6 V at 0.3 *C* CC charging. Note that *C*-rate is calculated based on theoretical capacity of used electrolyte (0.28 mA h). While the charging voltage is observed at similar value (2.6 V) with the expected cell voltage from cyclic voltammetry results (2.55 V), the working voltage is far below than expected value even with low *C*-rate (0.15 *C*). Differential capacity plot (Figure 18c) indicates that the discharge voltage is lying at 1.0 V of cell voltage, which is about 1.5 V lower than the cell voltage. To verify the origin of polarization at discharging, the GITT experiment is conducted. Since the cell voltage is expressed as electrochemical reaction quotient of electrolyte solution (from Nernst equation), the SOC at inert electrode surface can be traced by QOCV values from GITT experiment. Before

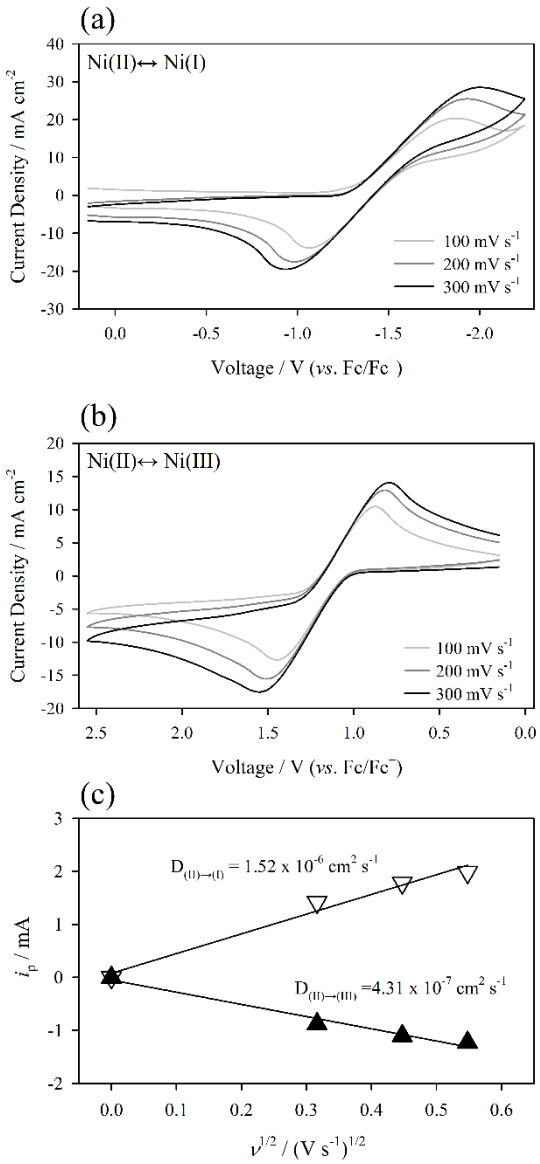

Fig. 16 Cyclic voltammograms recorded from 0.4 *M* Ni(II)(cyclam) dissolved 0.5 *M* $TEABF_4$ in EC/PC (1:1 = *v*/*v*) at (a); Ni(II) to Ni(III) and (b); Ni(II) to Ni(I). (c); Randles-Sevcik plots from Ni(II)(cyclam) redox reactions. The scan-rate-dependent peak current values are obtained from (a) and (b).

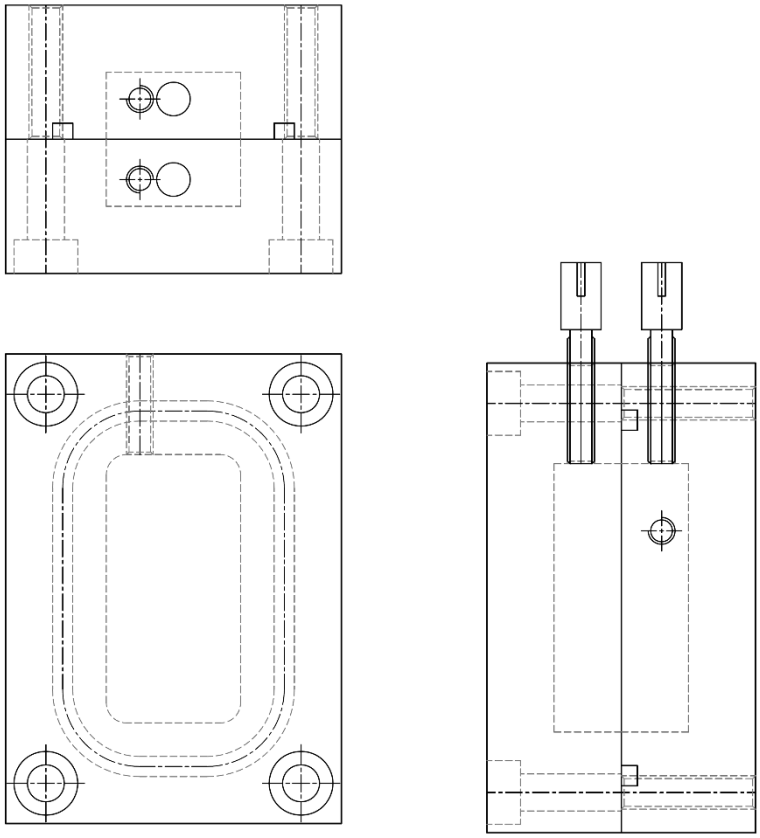

Fig. 17 Exploded view of homemade H-cell

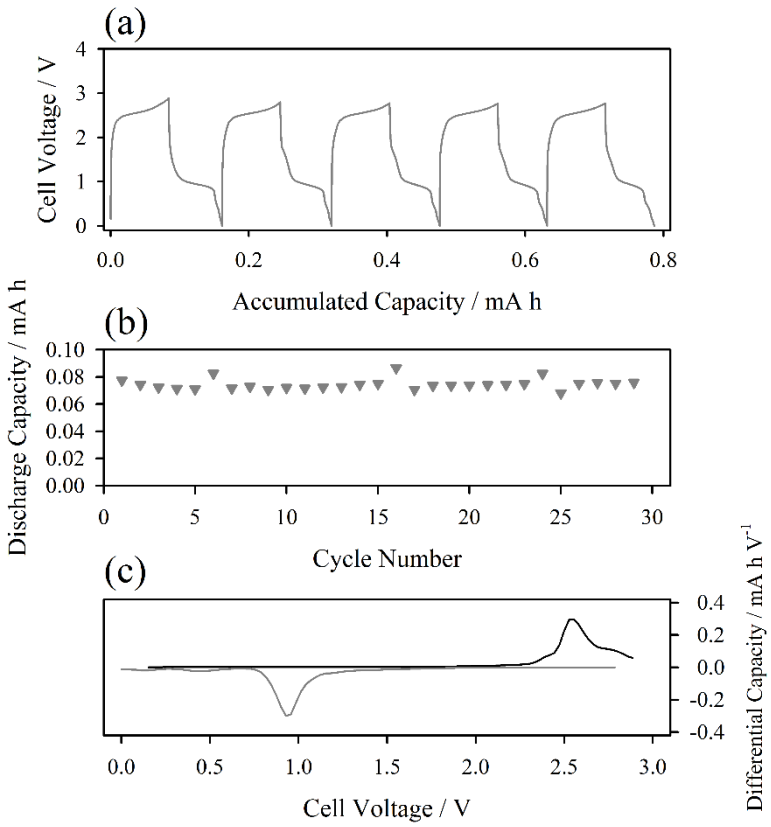

Fig. 18 (a); Accumulated capacity *vs*. cell voltage curves recorded from 10 m*M* Ni(II)(cyclam) dissolved 1.0 *M* $TEABF_4$ in EC/PC (1:1 = *v*/*v*) electrolyte at carbon paper/TEA^+ exchange membrane/carbon paper comprised H-cell. H-Cell was charged to SOC 30 and fully discharged (0.0 V voltage cut). (b); Cycleability of Ni(II)(cyclam) dissolved electrolyte and (c); 1st Differential capacity plot from (a). Currents are 0.3 *C* and 0.15 *C* CC for charging and discharging, respectively.

examination, the electrochemical mechanism of Ni(II)(cyclam) on carbon paper inert electrode is verified. If the current density increases with the square-root of scan rate, electrochemical reaction would be limited by diffusion of redox couples. **Figure 19**a shows the voltammogram at carbon paper working electrode. Since the increased current ratio is near square roots of five, the electrochemical mechanism on electrode surface is diffusion-limited. Thus, the surface concentration can be analyzed by QOCV values. The GITT plot at H-cell is demonstrated (Figure 19b) and QOCV values are converted into concentration ratio by Nernst equation. The inert electrode surface is mostly occupied with discharge species at any SOC (Figure 19c). Thus, the concentration overpotential is major deficiency for low energy efficiency. To reduce concentration overpotential of H-cell, the modified coin-cell experiment is conducted (Figure 19d). The reduced electrode-electrode distance can be achieved by coin-type cell. The stable voltage profile with 2.61 V for charging and 2.49 V for discharging is observed at coin-type cell. Polarization is about 60 mV at 50 $\mu A\ cm^{-2}$, which is slight higher than the value from Nernstian redox couples, theoretically (57 mV). Thus, the energy efficiency of redox couple can be maximized by optimizing cell configuration.

4.3.3 Further modification of counter anions for enhancement of solubility of complex cation

The solubility law indicates that the low melting point is preferred for higher solubility in ideal solution. Thus, the solubility of complex cation can be maximized from lowering lattice enthalpy, which is directly correlated with melting point [53]. Born-

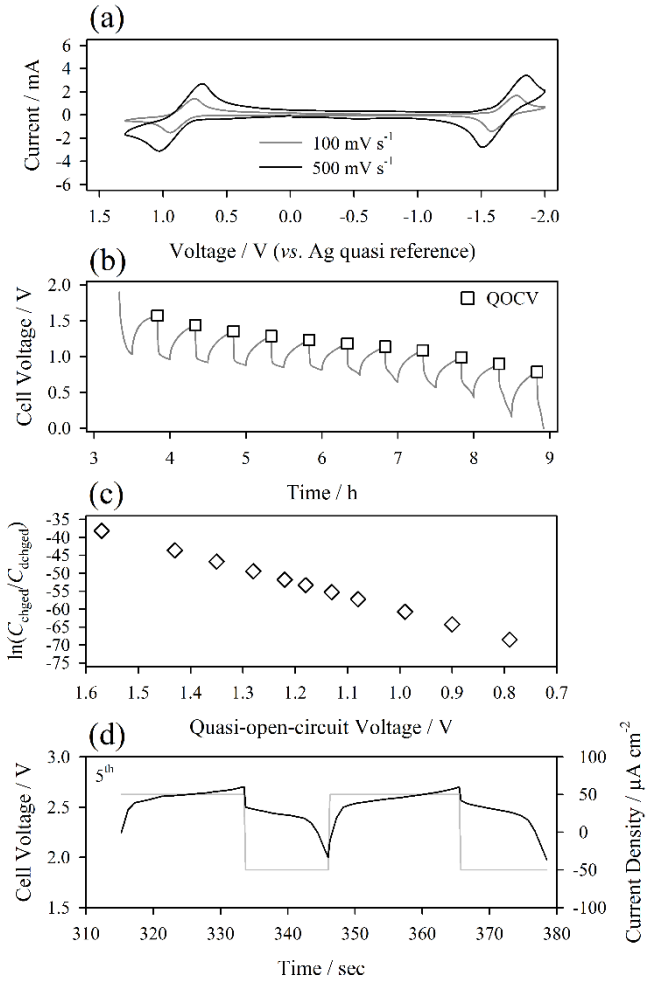

Fig. 19 (a); cyclic voltammograms obtained from 10 m*M* Ni(II)(cyclam) dissolved 1.0 *M* $TEABF_4$ in EC/PC (1:1 = *v*/*v*) electrolyte at carbon paper inert electrode. (b); Chronopotentiogram recorded at H-cell GITT experiment and (c); calculated concentration ratio at inert electrode surface from QOCVs. Current and rest period for GITT experiment are 10 min (current = 0.3 *C* CC) and 20 min, respectively. (d); Coin-type cell cycling at 50 μA cm^{-2}. Voltage cut-off = 2.0~2.7 V.

Mayer equation can be applied as rule-of-thumb. The equation is expressed as:

$$\Delta H_L \propto \frac{|Z_A Z_B|}{d_0}$$

where, ΔH_L is lattice enthalpy, z_i is charge of species i and d_0 stands for distance between ions. The solubility, therefore, is enhanced by enlarging diameter of anions because the lower melting point is expected from depressing lattice enthalpy of ionic solid. Sulfonate and imide anions are used as counter anions of lithium salt for lithium-ion batteries and room temperature ionic liquids from its high electrochemical stability at wide potential range [4, 54]. Thus, two anions, Tf^- and $TFSI^-$ are comprised as counter anions for Ni(II) complex cations. The measured solubility at supporting electrolyte is presented at **Figure 20**. Since the ionic radius is increased with ClO_4^- to $TFSI^-$ (Figure 20a), the solubility is enhanced by factor of two (Figure 20b). Note that working voltages (2.55 V) of ClO_4^-, Tf^- and $TFSI^-$ are identical because the mechanism of dissolution is same at three anions, dissociation.

The electrochemical stability of TFSI anion-attached complex cation is estimated by cyclic voltammogram. 10^{th} and 50^{th} electrochemical responses are shown at **Figure 21**a. The fully overlapped voltammogram is also observed at TFSI case, which is identical with ClO_4^- case. It is because the chemical and electrochemical stability of complex cation is largely influenced by the physical properties of complex cation. However, the solubility of redox couple is ruled by the selection of anion species. Thus, the design of complex cation can not only accomplished by complex cation, but also from counter

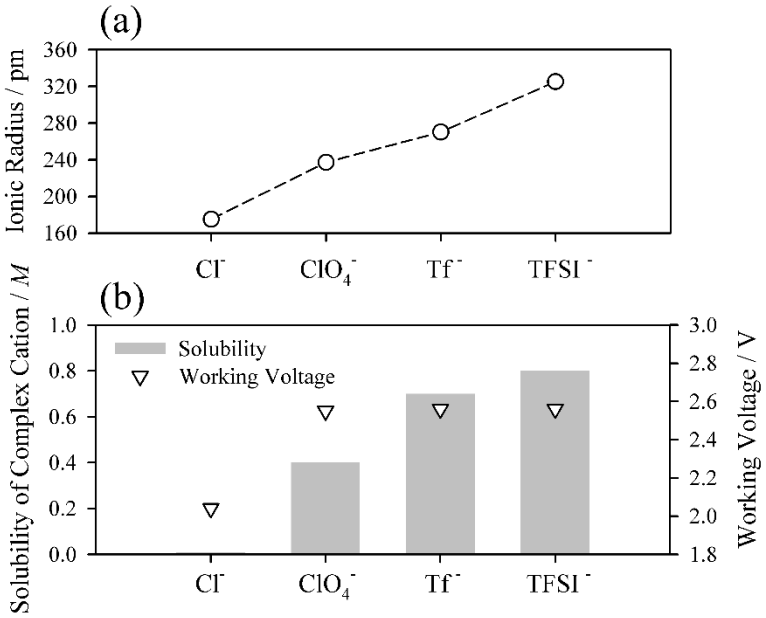

Fig. 20 (a); Ionic radius of various anions and (b); solubility and working voltage of Ni(II)cyclam complex cation with various counter anions at 1.0 *M* $TEABF_4$ EC/PC (1:1 = *v*/*v*) supporting electrolyte

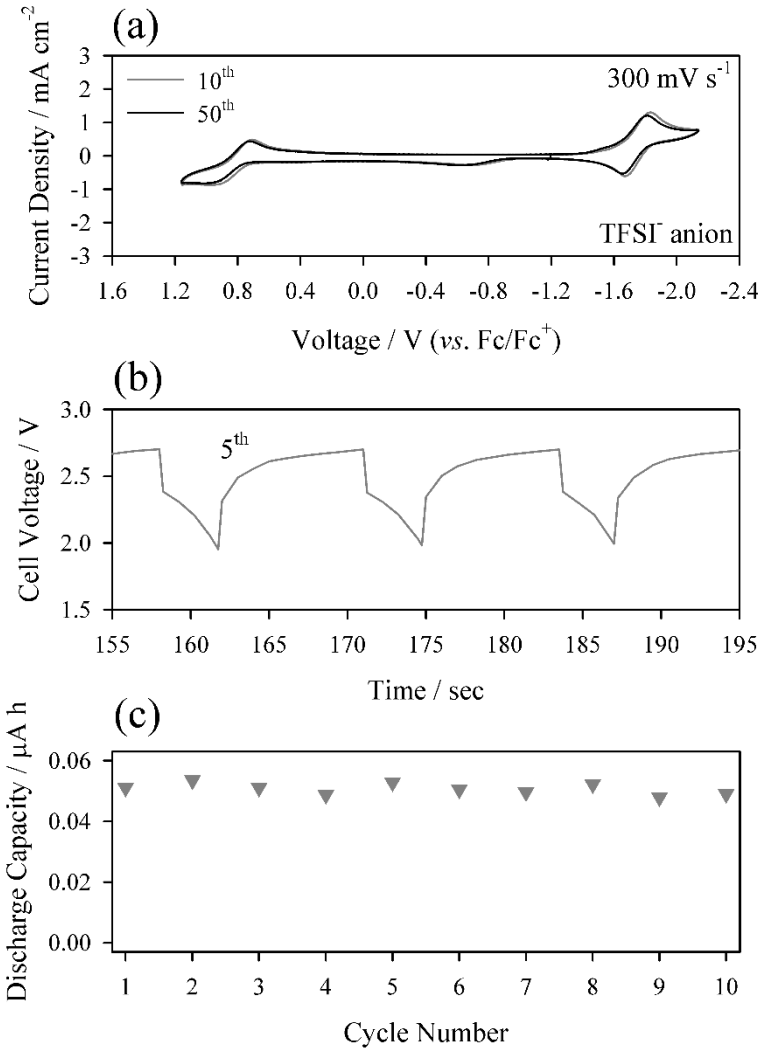

Fig. 21 (a); 10th and 50th cyclic voltammograms obtained at 10 m*M* Ni(II)(cyclam)[TFSI]$_2$ dissolved 1.0 *M* TEABF$_4$ in EC/PC (1:1=*v*/*v*) supporting electrolyte. (b); time *vs*. voltage curves from modified coin-cell configuration at 50 μA cm^{-2} and (c); cycleability from modified coin-cell. Voltage cut-off = 2.0~2.7 V.

anions. The modified coin-type cell cycling is conducted for TFSI-anion comprised RFB electrolyte (Figure 21b). The stable cycleability is also observed in Ni(II)(cyclam)$[TFSI]_2$ at coin-cell configuration.

4.4. Introduction of functional groups on redox couples for desirable dual functionalities as non-aqueous flow battery electrolytes

The electrochemically-generated permanent organic radicals are reported for several cases [29, 55]. Furthermore, several organic radicals exhibit intense color [56], which is promising for estimating SOC of flow batteries. However, the application of organic molecules on secondary battery systems are very limited in solid-state active material for lithium-ion [57] or sodium-ion battery [58] composite electrodes from the poor solubility of organic redox couples at non-aqueous solvents. Thus, the solubility increase of organic redox couple is crucial for applying organic materials as RFB electrolyte.

Another promising redox couples are metallocene-based materials [59]. Typical example is ferrocene, which is electrochemically and chemically stable because ferrocene accords 18 electron rule [60, 61]. Nevertheless, the solubility of ferrocene in polar non-aqueous solvents for dissolving salt is below average for practical applications. Furthermore, the redox potential of ferrocene (3.44 V *vs*. Li/Li^+) is somewhat insufficient as positive redox couple of RFBs. Therefore, the enhancement of both solubility and working voltage is crucial for ferrocene molecule.

Two approaches are conducted on organic and ferrocene redox couples. Firstly, the

type of secondary bonding is changed. It is because the heat of fusion and melting point are greatly influenced by the strength of interaction, *i.e.* hydrogen bonding or van der Waals interaction. Since the Carnelly's rule indicates that the asymmetric structure depresses melting point, functional groups are substituted on pristine molecules for increase of solubility, secondly.

4.4.1 Functional group effects on organic redox couples: solubility, chemical stability and redox potential

Organic redox couples begin to gain attention of material chemists recently because the potential effectiveness on the cost of secondary battery system [37]. The structure of organic redox couples can be divided into two moieties; conjugation backbone and redox centers. Since one electron can be reversibly transferred at each redox active functional groups at least, the total number of transferred electron into or out from redox couple can be determined by the number of redox-active functional groups. Therefore, the volumetric capacity of organic redox couple can be tailored by controlling the number of redox-active functional groups. However, the solubility drawback of organic redox couples limits the volumetric capacity of flow battery electrolytes.

Two organic redox couples, *p*-phenylendiamines and phthalimides are selected as positive and negative electrolyte, respectively. While two redox couples demonstrate the adaptable electrochemical properties as flow battery active materials, the solubility, redox potential and chemical/electrochemical stability are remained issues for *p*-

phenylendiamines and phthalimides as redox couples for RFBs. To enhance these electrochemical properties, the substitution effects on solubility, stability and redox potential are handled for these two organic redox couples, in sequence.

4.4.1.1 Methylation effects on solubility and stability of *p*-phenylenediamine-based positive redox couples

p-Phenylenediamine (PD) has two redox centers (amine groups) and low molecular weight (108.14 g mol^{-1}), which is desirable material characteristics for flow battery active materials. When this type of molecule is utilized as an active material for flow batteries, it is possible to generate the twice larger volumetric capacity than the case when there is only one electron involved in the redox reaction at same concentration, in theoretically. Nevertheless, low solubility (0.5 *M* in 1.0 *M* $LiBF_4$ in PC) and the lack of chemical reversibility are problematic issues for practical applications. The molecular structure of PD (inset of **Figure 22**a) shows that the redox centers (amine groups) have two disadvantages as flow battery active material. As aforementioned, the thermal properties such as melting point and heat of fusion can be detrimental factors for solubility of redox couples. Thus, the strong secondary bonding is not favorable for high solubility. However, the PD molecule has two hydrogen bonding centers, which are one of the strongest secondary interactions. Note that the N-H to N: hydrogen bonding is regarded as especially strong hydrogen bonding. Furthermore, the proton attached with nitrogen cannot shield effectively because the proton does not possess enough steric hindrance for electrochemically generated radical and dication. The

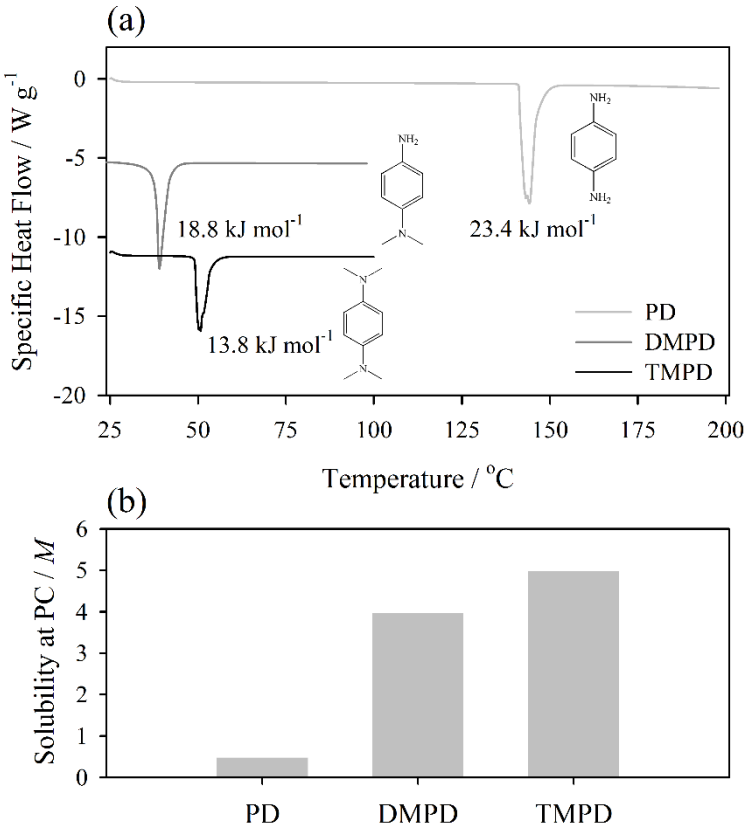

Fig. 22 (a); Differential scanning calorimetry (DSC) results from PD, DMPD and TMPD and (b); measured solubility of three molecules at 1.0 *M* $LiBF_4$ in PC supporting electrolyte.

thermal properties of PD can be enhanced by methylation of amine groups. By substituting proton to methyl groups, both high redox stability and solubility can be achieved because the hydrogen bonds from amines are eliminated and methyl groups can effectively shield redox centers. The thermal properties of PD derivatives are measured DSC, respectively (Figure 22a). The degree of methylation is different from PD to *N*,*N*-dimethyl-*p*-phenylenediamine (DMPD), *N*,*N*,*N*′,*N*′-tetramethyl-*p*-phenylenediamine (TMPD). The melting point of PD is depressed about 100 K at both molecules. However, the remained amine group at DMPD is manifested in heat of fusion. The solubility at 1.0 *M* $TEABF_4$ in PC supporting electrolyte is 5.0 *M* at TMPD and is inverse proportion to the number of hydrogen bonds (Figure 22b).

Since the ratio of cathodic and anodic peak currents demonstrates the chemical reversibility of redox couple, ratios from PD-derivatives show electrochemical and chemical stability of redox couples. **Figure 23** presents the cyclic voltammograms from three molecules and peak current ratios of 1^{st} and 2^{nd} redox reactions from voltammograms. Half-wave potentials of 1^{st} and 2^{nd} redox reactions from three molecules are nearly identical: $E_{1/2}$ = 3.2 V (*vs*. Li/Li^+) for the 1^{st} redox reaction and $E_{1/2}$ = 3.8 V (*vs*. Li/Li^+) for the 2^{nd} redox reaction. However, the redox stabilities of three molecules are quite different. While the peak current ratio from PD molecule is about 0.5 at both redox reactions, the ratio from TMPD is nearly unity. It is because the methyl group effectively shields the nitrogen redox centers. Thus, the electrochemical and chemical stability of redox couple is largely enhanced by methylation of amine groups, in sequence. The chemical degradation of electrochemically generated radicals

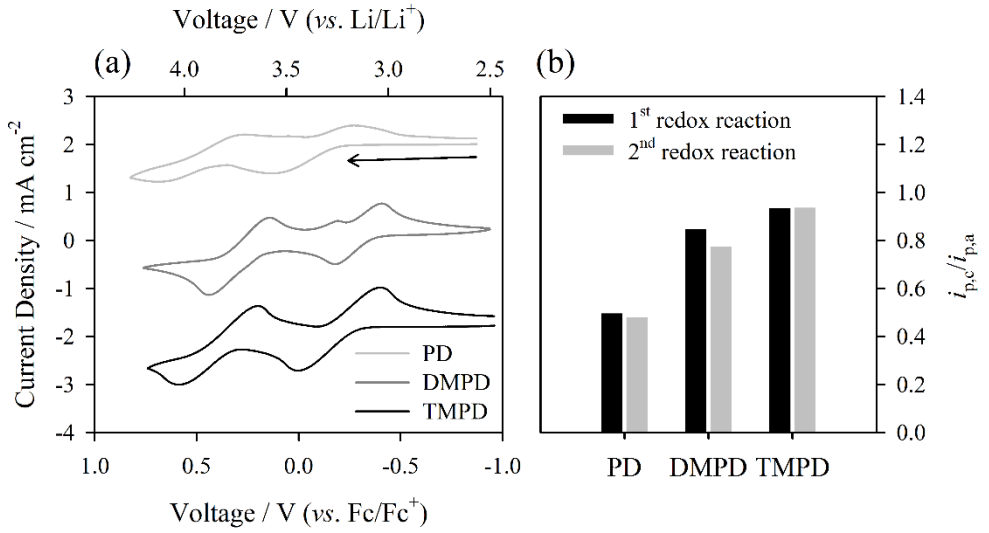

Fig. 23 (a); Cyclic voltammograms obtained from 10 m*M* of PD derivatives at 1.0 *M* $LiBF_4$ in PC supporting electrolyte. Scan rate = 100 mV s^{-1} (b); peak current ratios of three organic redox couples. The current values are from (a).

is from the chemical reactions between radicals, solvents and dissolved salts. Therefore, the introduction of steric hindrance on redox center is promising for enhancing radical stability in supporting electrolyte. In short, solubility and redox stability of three organic molecules are directly proportional to degree of methylation because the melting point and heat of fusion are decreased by eliminating hydrogen bonds and the foreign attack from surrounding is greatly suppressed by sterically hindered redox centers.

The chemical stability of redox couple is verified by computational method. The Dahn *et al*. suggest that the cycleability of radical cations can be estimated by binding tendancy of ethyl radical (*ER*) on radical molecule [62]. Furthermore, the proposed onset binding energy value for cycleability >100 is 1.73 eV. The computational estimation of PD, DMPD and TMPD molecule is conducted. The *ER* binding sites for three molecules are demonstrated at **Figure 24**a. The binding energy of radical cations should be compared because the values at literature is only for radical cations [62]. Only TMPD has lower value than onset value (1.73 eV) at all sites (Figure 24b). Thus, the chemical stability of fully-methylated TMPD is defined again as electrochemical results.

The repeated voltammograms obtained from TMPD dissolved electrolyte and scan-rate-dependent peak current ratio are presented at **Figure 25**. Very overlapped voltammograms are observed from TMPD electrolyte after 30^{th} redox reactions. Since the electrochemical reaction coupled chemical reaction (*EC* mechanism) in electrolyte solution is time-dependent at certain chemical rate constant, the electrochemical

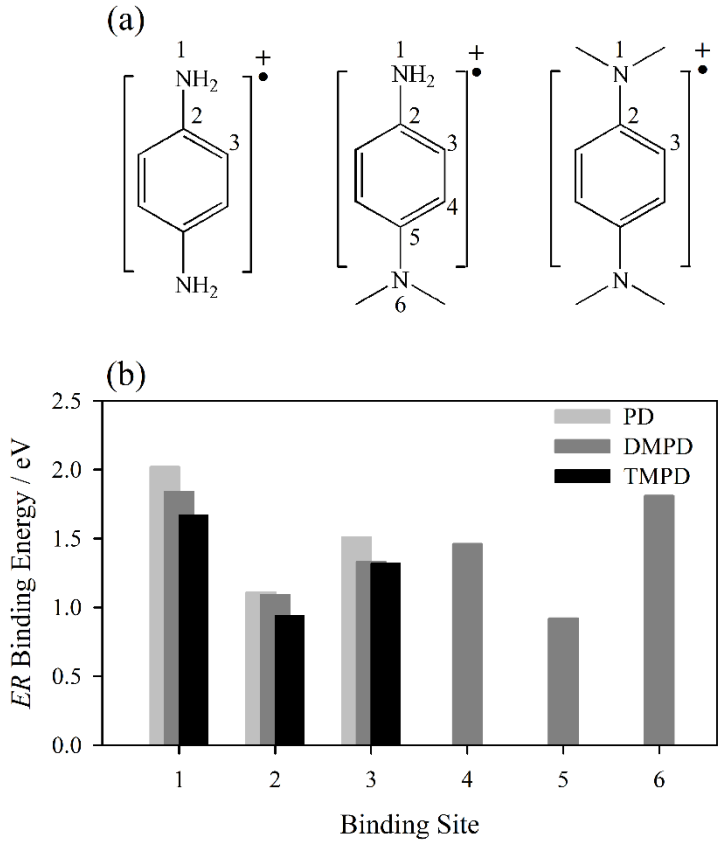

Fig. 24 (a); Ethyl radical (*ER*) binding sites for PD, DMPD and TMPD. (b); *ER* binding energies of three molecules from computational estimation.

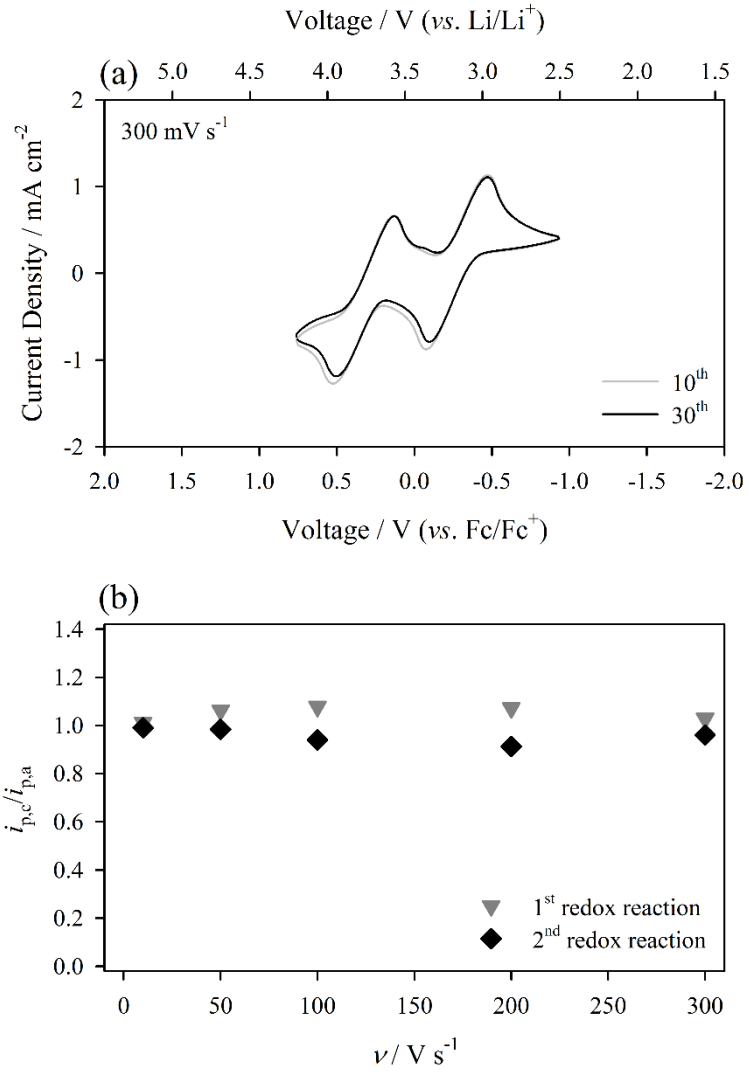

Fig. 25 (a); Cyclic voltammograms obtained from multiple-scanning 10 m*M* TMPD dissolved 1.0 *M* $LiBF_4$ in PC supporting electrolyte. (b); peak current ratio *vs*. scan rate of TMPD dissolved electrolyte

reaction mechanism can be traced by plotting peak current ratio *vs*. scan rate. If there is electrochemical reaction coupled chemical reaction in electrolyte solution, the peak current ratio will be low at slow scan rates. It is because the reverse peak currents from slow voltage scan is the most time-spending sweep. Nonetheless, the peak current ratios are unity at performed all scan rates. Again, the chemical stability of TMPD is electrochemically verified.

Diffusion coefficients of TMPD and oxidized TMPD molecule are calculated by Randle-Sevcik plot. Furthermore, Randle-Sevcik plot approves the chemical reversibility of redox couple because the assumption of this equation for analysis is chemically reversible redox couple. **Figure 26** presents the scan-rate-dependent voltammograms and derived Randle-Sevcik plot of TMPD and TMPD radical cation. Since peak potentials are shifted with increase of scan rate, the electrochemically irreversible case is applied for calculating diffusion coefficients, as Ni(II)cyclam. The Randle-Sevcik plots from both TMPD and radical cation clearly indicate that the two molecules are chemically reversible because the scan rate *vs*. peak current plots obey Randle-Sevcik equation. Calculated diffusion coefficients are in the range of 10^{-6} cm^2 s^{-1} and those values are sufficient high in non-aqueous electrolyte, also [52]. Therefore, good rate performance is expected at TMPD-dissolve electrolyte from the sophisticated diffusion rate of TMPD.

The galvanostatic non-flowing coin-cell cycling is conducted for proof-of-concept of TMPD. This type of cell is not ideal for estimating flow battery electrolyte, however, the chemical stability and electrochemistry of TMPD can be demonstrated by this cell.

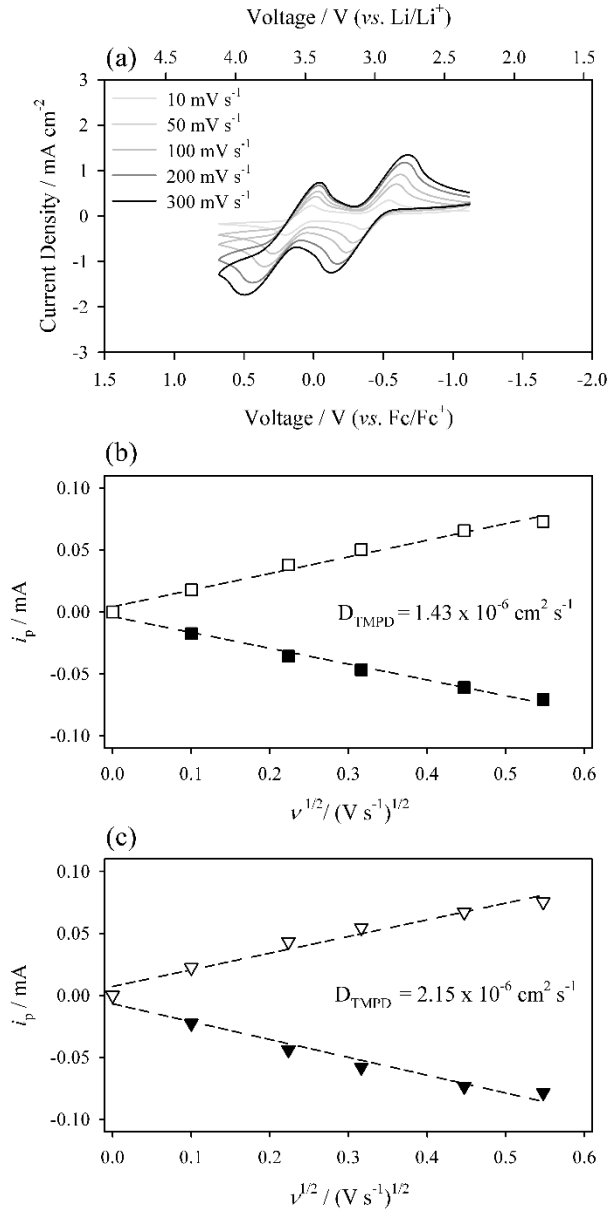

Fig. 26 (a); Scan-rate-dependent cyclic voltammograms obtained from TMPD dissolved PC-based electrolyte and peak current *vs*. scan rate$^{1/2}$ plot for (b); TMPD ↔ TMPD$^{+\cdot}$ and (c); TMPD$^{+\cdot}$ ↔ TMPD^{2+} redox reactions. The peak current values are derived from Fig. 26a. The scan rates are indicated in the inset.

Figure 27 presents the time-voltage curves and cycleability from TMPD-dissolved electrolyte at Li-half cell. The voltage profile demonstrates very stable two plateaus. Half-points of two voltage plateaus are located at 3.2 and 3.8 V (*vs*. Li/Li^+), respectively. Two voltages are equivalent with the expected cell voltages from cyclic voltammetry results. Thus, TMPD molecule can store twice higher capacity than single redox reaction-involved redox couples at same concentration. The cycleability of TMPD after several stabilization period is shown at Figure 27b. The stable cycle performance over 400 cycles is observed at TMPD-dissolved electrolyte. In short, the methylation of amine groups in PD molecule is dual-functional substitution. The steric hindrance on nitrogen molecule gives very stable chemical stability and elimination of hydrogen bonding of NH_2 to :N enhances solubility of redox couple. The high solubility (5.0 *M*) and working voltage (3.2 and 3.8 V *vs*. Li/Li^+) are achieved, resulting 938 W h L^{-1} of energy density.

4.4.1.2 Introduction effects of aliphatic chain on solubility and redox potential of phthalimide-based negative redox couples

Since *N*-methylphthalimide (MPI) has ketone functional groups in molecular structure, highly stable ketyl radical can be generated by electrochemical reduction of organic molecule. Therefore, MPI can be applied as negative redox couple for flow batteries [12]. However, Li *et al.* reports that the solubility of MPI is limited (0.1 *M*) in acetonitrile-based electrolyte. Solubility of MPI is also limited in propylene carbonate solvents (0.5 *M*), also. Therefore, the great sacrifice of volumetric capacity is expected

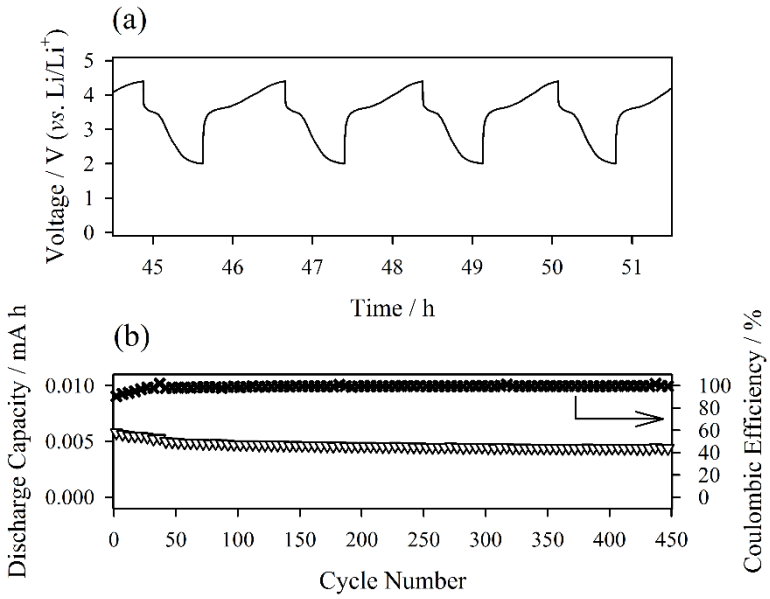

Fig. 27 (a); Time-voltage curves of 0.1 *M* TMPD/Li coin-type non-flowing cell and (b); cycleability and Coulombic efficiency after a stabilization period. Current density = 10 μA cm^{-2}. Voltage cut-off = 2.0~4.3 V (*vs*. Li/Li^+)

by MPI-dissolved electrolytes. The functional group introduction can resolve the solubility problem of MPI. Moreover, the substitution of phthalimides is easily prepared by S_N2 reaction with potassium phthalimide and alkyl halides [63]. However, the introduction of proper functional group is important for obtaining physicochemical and electrochemical properties. Carnelley's rule, established by Thomas Carnelley in 1882, indicates that the degree of molecular symmetry is correlated with melting point of organic solid. Since the high solubility of redox couple is resulted at low melting point, asymmetric structure is favorable at phthalimide negative redox couple. The molecular structures of MPI is presented at inset of **Figure 28**. While the butyl-attached phthalimide is very asymmetric by long aliphatic chain, the MPI has highly symmetric molecular structure. Thus, ineffective electron interaction is expected at *N*-butylphthalimide (BPI) molecule. The thermal properties of two solids are measured by DSC. The melting point is greatly decreased by 100 K at butyl-attached case. Furthermore, from the ineffective secondary interaction, the heat of fusion is also decreased by butyl-substitution. From decrease of melting point and heat of fusion, the higher solubility is predicted from solubility equation at BPI. The measured solubility at 1.0 *M* $TEABF_4$ in PC supporting electrolyte reaches 5.0 *M* at butyl-substituted phthalimides. The solubility is ten-fold increased by increasing the length of aliphatic chain attached at nitrogen atom. The theoretical volumetric capacity of BPI reaches 134 A h L^{-1} at carbonate-based supporting electrolyte. Also note that this value is one of the most highest capacity from non-aqueous flow battery electrolytes [31].

Redox potential of redox couple is also crucial for flow battery application because

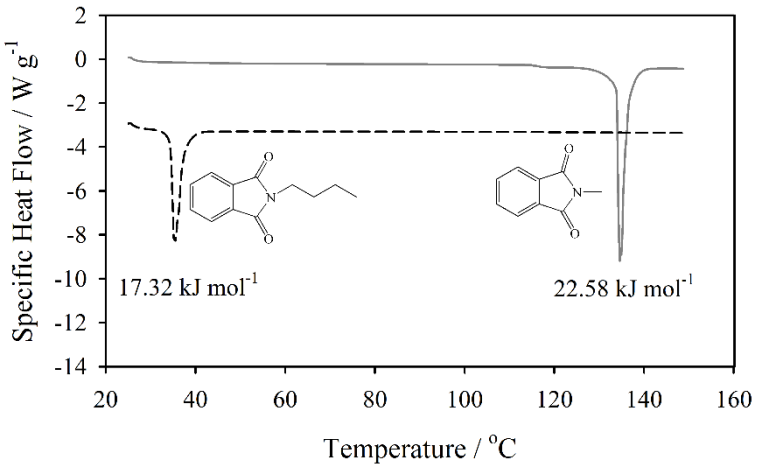

Fig. 28 Differential scanning calorimetry (DSC) results from *N*-methylphthalimide and *N*-butylphthalimide. Molecular structures are indicated at inset.

the energy density of flow battery electrolyte is multiple of working voltage and volumetric capacity. Since the aliphatic chain is well-known electron-donating group, the negative lift of working voltage is also expected by butyl substitution. The cyclic voltammgram of two phthalimides are presented at **Figure 29**. Note that the peak current values of two molecules are very similar at same concentration. It is because the worsening of electrochemical kinetics is not resulted by long aliphatic chain. The redox potential is 0.1 V negative lifted by long butyl chain because the electron-donating effect and solvation change from lengthening aliphatic chain of redox couple shift redox potential. The solvation change of redox couple after electrochemical reaction affects the redox potential and additional solvation factor is imposed by long aliphatic chain [64, 65]. Rather non-polar organic redox couple (BPI) goes through with severe solvation change in polar solvent, resulting low reduction potential. Finally, redox potential of BPI from half-wave potential reaches -1.92 V (*vs*. Fc/Fc^{+}).

Chemical stability of redox couple is necessity for flow battery electrolyte because the stability is directly correlated with cycleability. The repeated voltammograms and scan-rate-dependent peak ratios are plotted for BPI molecule. **Figure 30** demonstrates results from BPI-dissolved electrolyte. Very overlapped voltammograms are observed even after 50^{th} scan of BPI electrolyte (Figure 30a). Thus, the chemical stability of BPI is sufficiently high for flow battery application. The further examination of BPI is conducted by scan rate *vs*. peak current ratio plot. The degradation in peak current ratio at slow scan rate is not observed at BPI electrolyte because the *EC* mechanism does not stand for BPI redox couple. Therefore, the butyl group introduction on phthalimide

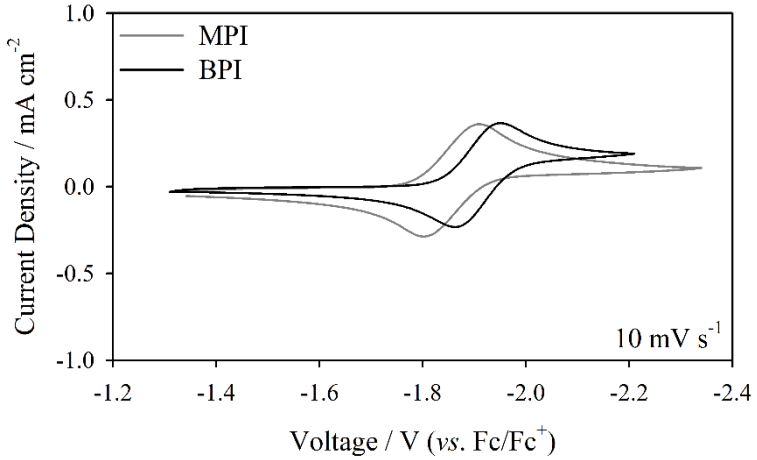

Fig. 29 Cyclic voltammograms obtained from 10 m*M* of *N*-methyl and butylphthalimide dissolved 1.0 *M* $TEABF_4$ in PC supporting electrolyte at 10 mV s^{-1} scan rate.

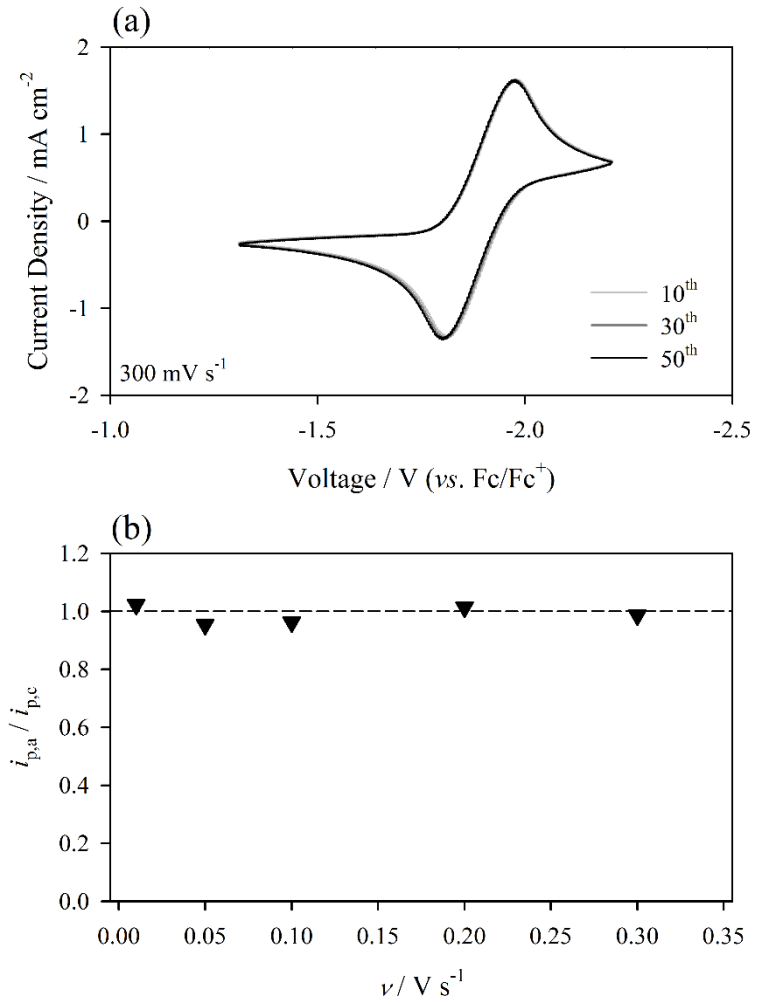

Fig. 30 (a); Cyclic voltammograms obtained from multiple-scanning 10 m*M* *N*-butylphthalimide dissolved 1.0 *M* $TEABF_4$ in PC supporting electrolyte. (b); peak current ratio *vs*. scan rate of *N*-butylphthalimide dissolved electrolyte

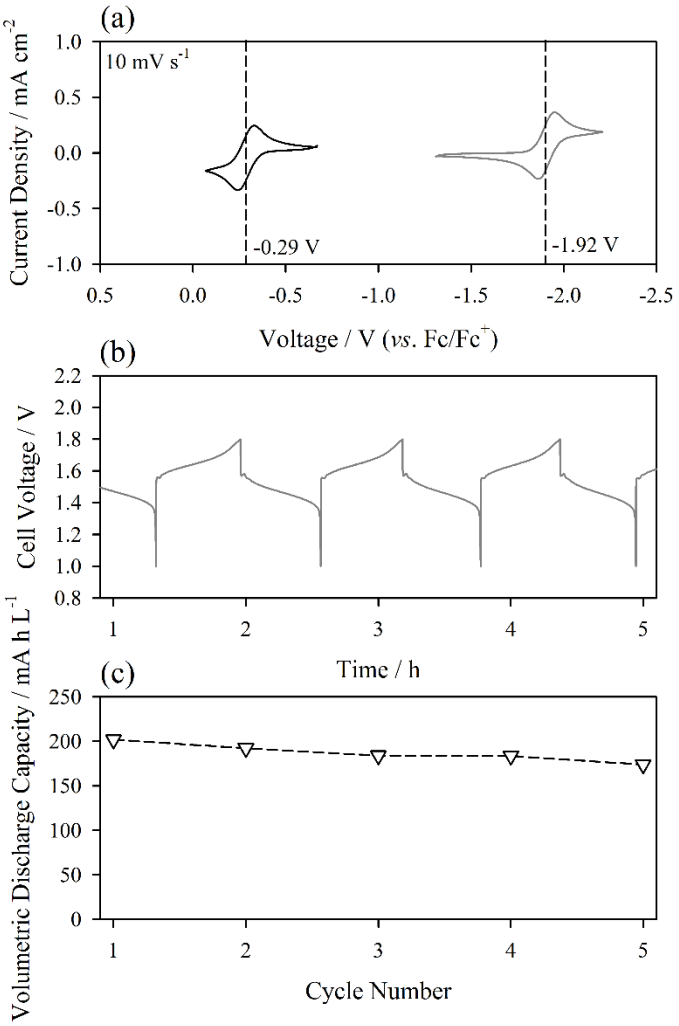

Fig. 31 (a); Cyclic voltammograms obtained from 10 m*M* TMPD and BPI dissolved electrolyte at 10 mV s^{-1} scan rate. (b); time-voltage curves of 0.1 *M* TMPD and 0.1 *M* BPI dissolved electrolyte and (c); cycleability of TMPD/BPI flowing cell. Charge/discharge currents were 40 mA and flow rate was 20 RPM. Voltage cut-off = 1.0~1.8 V.

molecule is bifunctional; increase of both working voltage and solubility.

The galvanostatic charge-discharge experiment of TMPD/BPI electrolyte comprised all-organic RFB is conducted at KETI. **Figure 31** presents the results. The expected cell voltage is 1.63 V for TMPD with one electron-involved redox reaction at N/P =1, (Figure 31a). Voltage profile obtained from equivalent amount of TMPD and BPI has the cell voltage at 1.6 V region, which is the expected cell voltage from cyclic voltammogram (Figure 31b). The cycleability is very stable with 5^{th} repeated cycles and the theoretical energy density of all-organic RFB is 117.3 W h L^{-1} at fully utilized two redox reactions of TMPD; thereby allowing higher energy density than aqueous RFB (typically 15.0 ~ 25.0 W h L^{-1} for VRFB).

Two organic molecules, TMPD and BPI are rationally designed by tailoring thermal properties of solid materials. Designed all-organic RFB not only has high energy density, but also owns cost-effectiveness from cheap organic redox couple. Therefore, all-organic RFB possesses further advantages as large-scale ESSs [66].

4.4.2 The effects and plausible mechanism of acetyl group introduction on ferrocene for non-aqueous Li-flow battery

Ferrocene (Fc) as the redox couple for flow battery application is not favorable from its relatively low redox potential (3.44 V (*vs*. Li/Li^+)) and low solubility in non-aqueous solvents, especially, 0.04 ~ 0.2 *M* at mixed carbonate solvents [59, 67]. Nevertheless, Fc is regarded as a potential candidate for flow battery electrolyte from its high electrochemical and chemical stability of redox couples even in the various organic

solvents [27]. Furthermore, Fc is one of the well-known metal-ligand complexes, which is contented with the 18 electron rule [59, 60]. By the satisfaction of this rule, the storage of the active material at the ambient condition is possible. Since the main applications of the flow battery are large-scale ESSs, the storage and maintenance of the electrolyte solution cannot be accomplished in the perfectly air and moisture-free from its scale. Thus, this characteristic leads Fc to promising candidate of active material of RFBs. Since the working voltage and solubility are not enough for practical applications, the enhancements of these two properties of Fc are largely demanded. The functionalization of Fc is effective approach for both increase of solubility and working voltage because the substitution of hydrogen to certain functional groups on cyclopentadienyl ligands is readily available by Friedel-Crafts method [68].

At first, proper functional groups for Fc must be selected for enhancing electrochemistry and solubility of pristine Fc molecule because the introduction of functional groups results the increment of the molecular weight; thereby increase strength of intermolecular interaction, resulting degradation of energy density. Thus, the selection of appropriate functional group is crucial for enhancing physicochemical and electrochemical properties of pristine molecule.

The solubility of redox active species affects by two large factors [69]. One is the interaction between solutes and the other is the strength of solute-solvent interaction. Those two factors are must be properly handled by the functional group modification of solute because the disappearance of interaction between solute molecules participates the dissolving process of solid materials. In short, the weak interaction

strength of solutes is desirable for high solubility. The thermal property, especially the melting point of solid can be a barometer for interpreting strength of interaction. In this viewpoint, the functional group effect on pristine molecule can be traced by those thermal parameters.

Ideal solubility equation clearly presents that both low melting temperature and enthalpy of fusion of solute molecule are desirable for high solubility. The practical approach can be inspired by the empirical rule, the Carnelley's rule [70]. The rule indicates that the low molecular symmetry leads depression of the melting point of the chemical compounds. The empirical rule signifies that the altered packing efficiency can act as the melting point depressor. Thus, the asymmetric molecular structure is demanded for better solubility of pristine molecule by reducing interaction strength between solutes.

Not only the weakened solute interaction, but also the strengthened interaction between solute-solvent molecules is important for high solubility. The solvent nature also affects the solubility by *"the like dissolves the like"* rule [71]. The organic solvent for non-aqueous flow battery systems must be high-polar and dielectric solvents because the use of charge carrier such as the lithium, sodium and alkylammonium salts is inevitable for the formation of the closed-loop of the cell [4]. To reinforce the interaction between solute and solvent molecules, therefore, the introduction of polar functional groups might be right direction. In short, to use Fc as the active material for the flow batteries, the introduction of the polar and asymmetric functional group is an appropriate direction from solute-solvent compatibility. The acetyl group is one of the

possible selections for those properties. Acetyl group can modify not only the solubility of Fc by less-symmetric structure and polarity, but also the redox potential of the Fc. HOMO level is down-stream shifted by the strong electron-withdrawing effect of acetyl groups, resulting the higher redox potential than that of Fc. In summary, the acetyl group composes less-symmetric structure than Fc with electron-withdrawing groups, resulting increase of the redox potential and solubility. Those two properties can improve energy density of pristine Fc molecule. The acylation of Fc is well-established by the Friedel-Crafts method [68]. Therefore, AcFc can be a promising candidate for flow batteries by its potential ability and the easiness of the preparation. The major concern is to define the applied equation and suggested redox couples followed could be applied as the factor for design of redox couples for flow batteries. To identify the predicted result is observed with AcFc electrolyte, the DSC and electrochemical analysis is preceded for validation. Furthermore, to define the reversibility of redox reaction, the coin-cell cycling of AcFc is conducted for Li-flow battery applications.

Measured solubility of AcFc at 1.0 *M* $LiPF_6$ dissolved PC electrolyte is 0.81 *M* and this value is 4.3-fold higher than solubility of pristine ferrocene. **Figure 32** presents the DSC results of Fc and AcFc. The melting point of ferrocene is greatly depressed about 100 K by acetyl substitution and the solubility equation indicates that near four-fold increase of solubility. Therefore, the increase of solubility is resulted from the depression of melting point of ferrocene.

To verify increment of working voltage, the cyclic voltammograms are obtained from

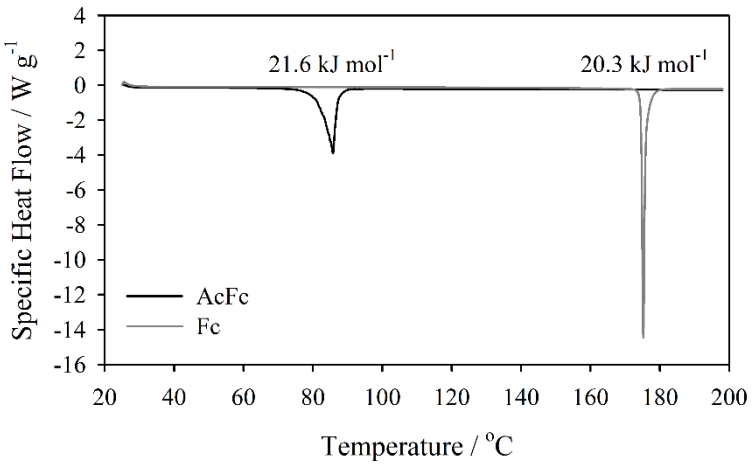

Fig. 32 Differential scanning calorimetry (DSC) results from acetylferrocene (AcFc) and ferrocene (Fc)

Fc and AcFc-dissolved electrolyte, respectively. **Figure 33** shows the voltammograms from AcFc and Fc. The redox potential is 0.21 V positive lifted by acetyl substitution, which is from the electron-withdrawing effects of acetyl group. The working voltage from cyclic voltammogram is 3.65 V (*vs*. Li/Li^+). The theoretical energy density of Li-flow battery with AcFc positive electrolyte reaches 79.2 W h L^{-1}.

Since the cycleability of flow batteries is dependent on the redox stability of used redox couple, the chemical and electrochemical stability of redox couple is crucial for cycle performance of RFB. The chemical and electrochemical stability of AcFc is examined by repeated cyclic voltammetry and scan rate *vs*. peak current ratio plot. **Figure 34** presents those results. Figure 34a demonstrates that the repeated scanned voltammogram for AcFc at the scan rate of 300 mV s^{-1}. Voltammograms indicate that no sign of the additional current peak generation and distortion of peak potential originate from repeated redox reactions; thereby the chemical stability of AcFc is defined. The cathodic/anodic peak current ratio demonstrates the electrochemical mechanism of AcFc. If an *EC* mechanism stands, the peak current ratio should be decreased at slower scan rates with fixed rate constant of chemical reaction. As demonstrated at Figure 34b, the sign from *EC* mechanism is negative for AcFc. Thus, the stable redox chemistry is expected at AcFc-dissolved electrolyte.

As aforementioned, the facile diffusion is important characteristic for rate capability of RFB because the heterogeneous charge transfer at inert electrode surface is diffusion-controlled. The diffusion coefficient of AcFc is measured by Randle-Sevcik plot and compared with Fc. The scan-rate-dependent voltammogram from AcFc

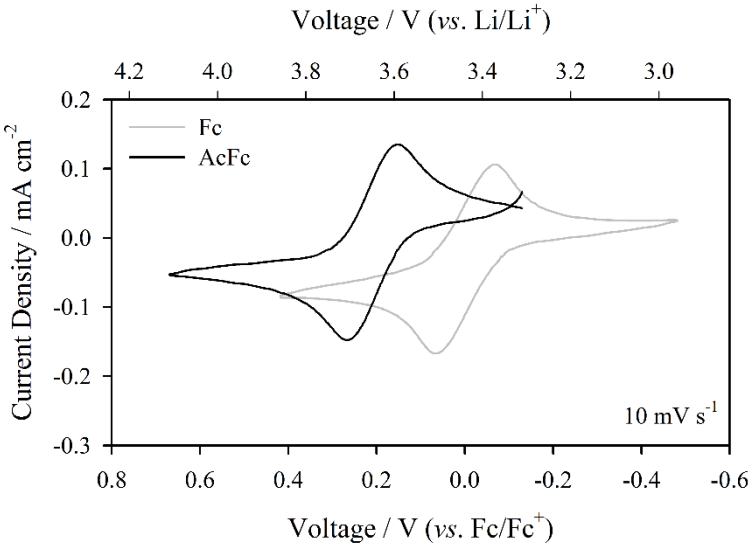

Fig. 33 Cyclic voltammograms obtained from 10 m*M* of AcFc and Fc dissolved 1.0 *M* $LiPF_6$ in PC supporting electrolyte at 10 mV s^{-1} scan rate.

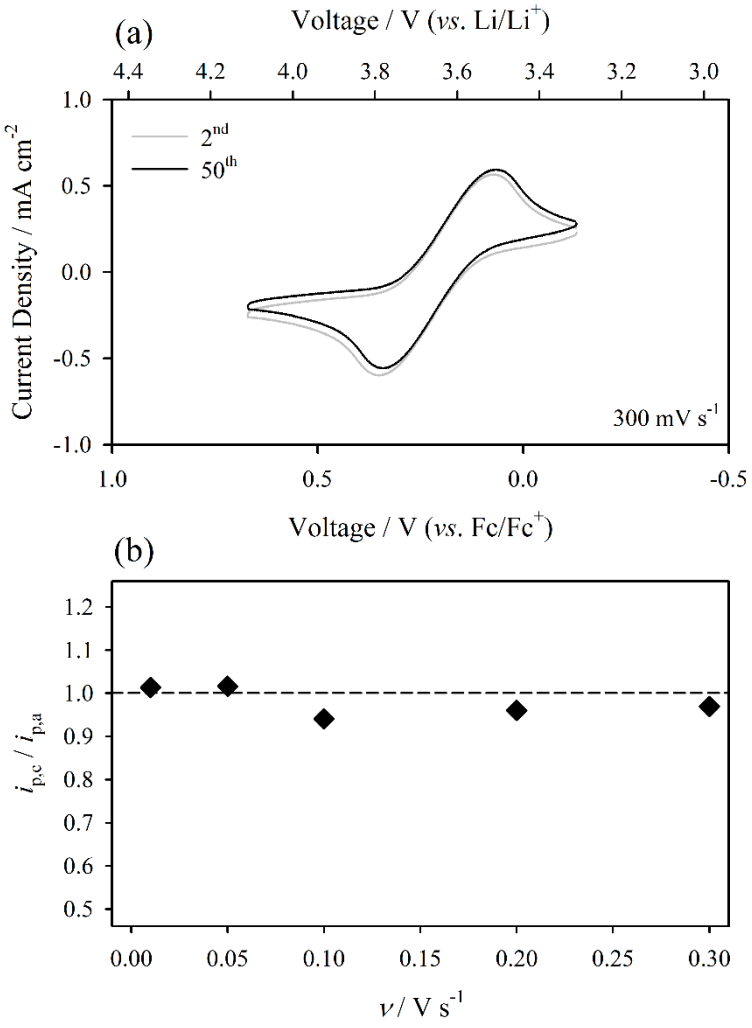

Fig. 34 (a); Cyclic voltammograms obtained from multiple-scanning 10 m*M* AcFc dissolved 1.0 *M* $LiBF_4$ in PC supporting electrolyte. (b); peak current ratio *vs*. scan rate of AcFc dissolved electrolyte

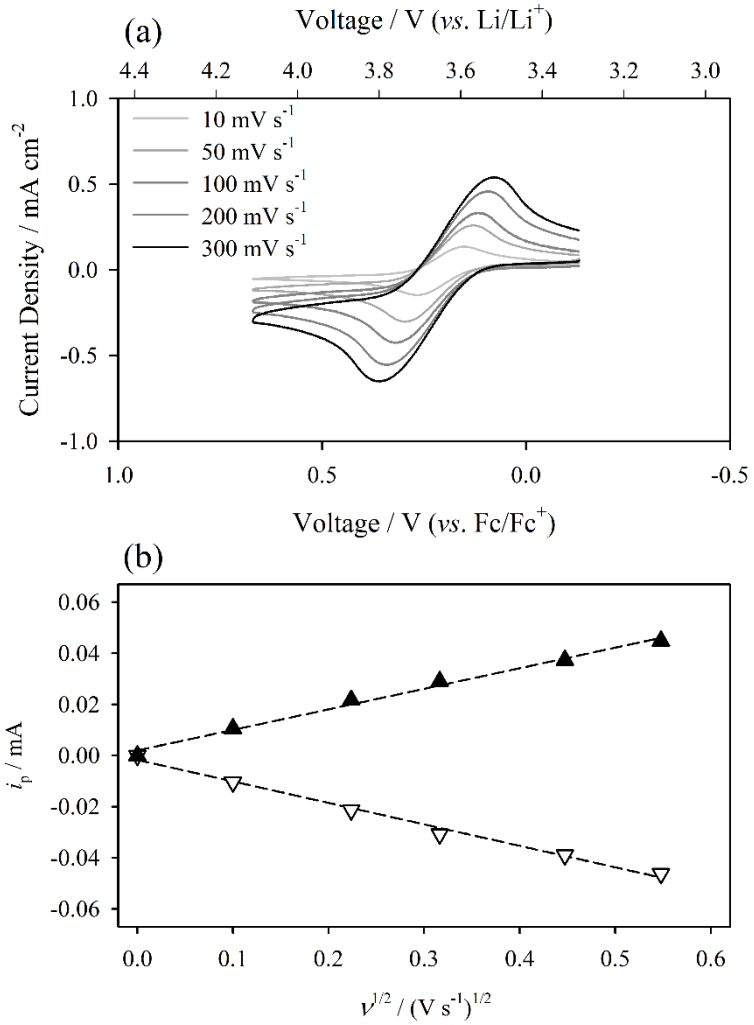

Fig. 35 (a); Scan-rate-dependent cyclic voltammograms obtained from AcFc dissolved PC-based electrolyte and (b); peak current *vs*. scan rate$^{1/2}$ plot for AcFc ↔ AcFc^{+} redox reaction. The peak current values are derived from Fig. 35a. The scan rates are indicated in the inset.

electrolyte shows peak potential shift with scan rate increase (**Figure 35**a). Therefore, the Randle-Sevcik equation for electrochemically irreversible case is applied for calculating diffusion coefficients. The diffusion coefficient of AcFc is 4×10^{-7} cm^2 s^{-1}, which is the similar value with the diffusion of the previous reported Fc derivatives, despite of enlarged molecular size [67].

Since the mechanism of charge transfer from inert electrode is electron-tunneling, the enlarged molecule size can be a detrimental factor for charge transfer by its distance from electrode surface. The comparison of polarization of AcFc and Fc is shown at **Figure 36**. Note that the current values are very similar with both AcFc and Fc at voltammetric results (Figure 33). The polarization is calculated by below equation:

$$Polarization = E_{p,a} - E_{1/2}$$

where, the $E_{p,a}$ is anodic peak potential. The polarizations from two redox couples are not quite different even at fast scan rates. Therefore, the acetyl-substitution does not hinder electrochemical reaction.

The modified 2032 coin-cell configuration is applied for proof-of-concept of the electrochemistry of AcFc for the Li-flow battery application. **Figure 37**a presents the time-voltage curves of the 0.5 *M* AcFc/Li cell. The cyclic voltammogram reveals that the redox reaction of AcFc occurs at the 3.65 V (*vs*. Li/Li^+). The voltage at half-point of charging and discharging plateaus also shows the consistent result from the expected cell voltage from cyclic voltammetry. However, in concentrated electrolyte (0.5 *M*), the

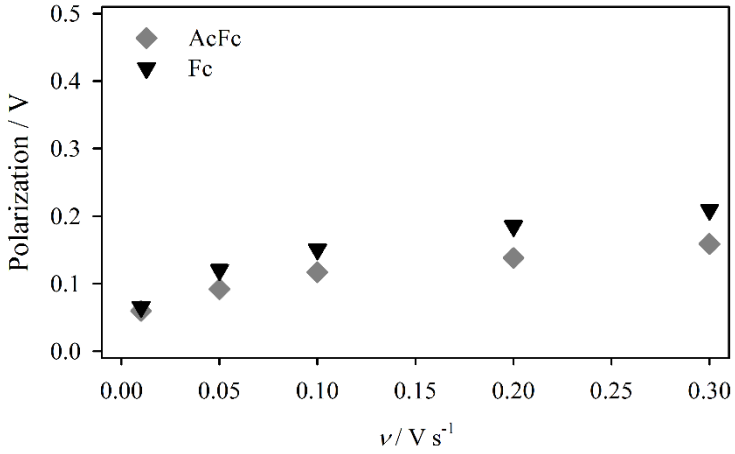

Fig. 36 Polarization *vs*. scan rate of 10 m*M* AcFc and Fc dissolved 1.0 *M* $LiPF_6$ in PC supporting electrolyte, respectively

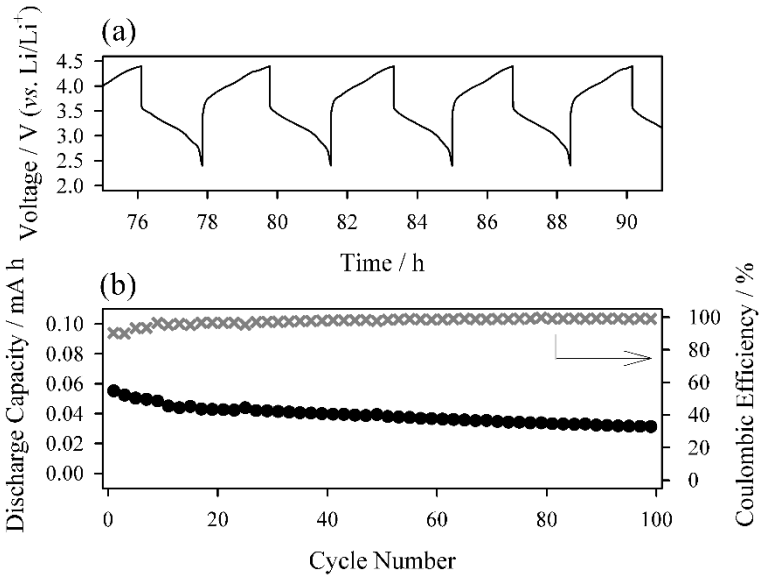

Fig. 37 (a); Time-voltage curves obtained from 0.5 *M* AcFc/Li coin-type non-flowing cell and (b); cycleability and Coulombic efficiency after a stabilization period. Voltage cut-off = 2.4~4.4 V (*vs*. Li/Li^+). Current density = 30 μA cm^{-2}.

gradual degradation of discharge capacity is observed after stabilization period. Since the electrochemical and chemical stability of AcFc are approved by cyclic voltammetry experiment of AcFc, the static cell condition is the source of degradation. The gradual cross-contamination of AcFc is one of possible reasons because concentration gradient of AcFc is sufficient high for cross-contamination at 0.5 *M* AcFc electrolyte [36, 72]. To verify the cross-contamination effects, 0.1 *M* AcFc electrolyte is galvanostatically cycled. **Figure 38** demonstrates the results from cycling of 0.1 *M* AcFc electrolyte. The voltage profile also provides the stable cell voltage at 3.65 V (*vs*. Li/Li^+) (Figure 38a). The remarkable result is the stable cycleability of 0.1 *M* AcFc electrolyte. Thus, the gradual degradation of discharge capacity of AcFc at concentrated electrolyte is from static cell configuration. The redox stability of AcFc leads the stable cycleability with 400 cycles, which is the promising ability for large-scale battery application; thereby the potential ability for flow battery application can be expected. The Coulombic efficiency exceeds 98% after 5 cycles, even in a non-optimized and non-flowing system.

To trace electrochemical charge-discharge mechanism of AcFc, the electron spin resonance spectroscopy (ESR) experiment is conducted. The orbital structure of AcFc is shown at **Figure 39**. As aforementioned, the AcFc is contented with 18 electron rule. After electrochemical oxidation, the unpaired electron is electrochemically generated. Therefore, the acetylferrocenium ($AcFc^+$) is ESR active. Post-mortem analysis of AcFc electrolyte is conducted at H-cell. **Figure 40** presents the time vs. voltage curves and ESR spectra from three indicated points. At pristine, no ESR signal is observed

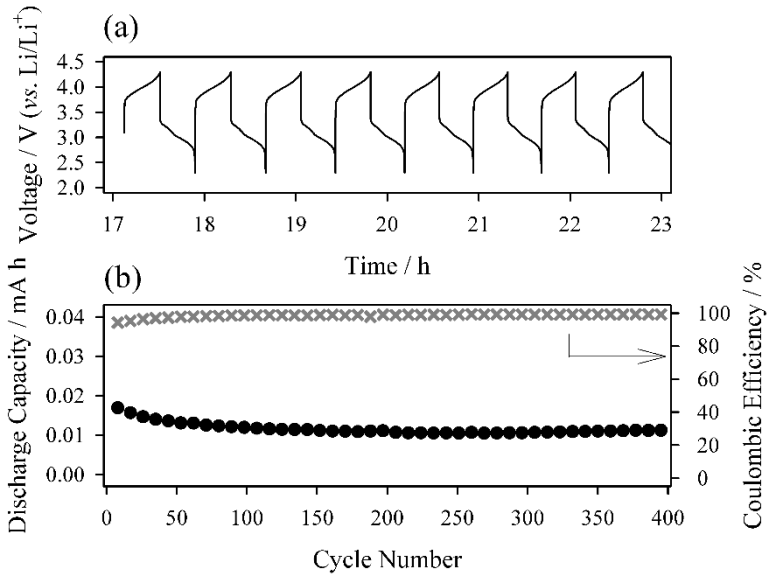

Fig. 38 (a); Time-voltage curves obtained from 0.1 *M* AcFc/Li coin-type non-flowing cell and (b); cycleability and Coulombic efficiency after a stabilization period. Voltage cut-off = 2.4~4.4 V (*vs*. Li/Li^+). Current density = 30 μA cm^{-2}.

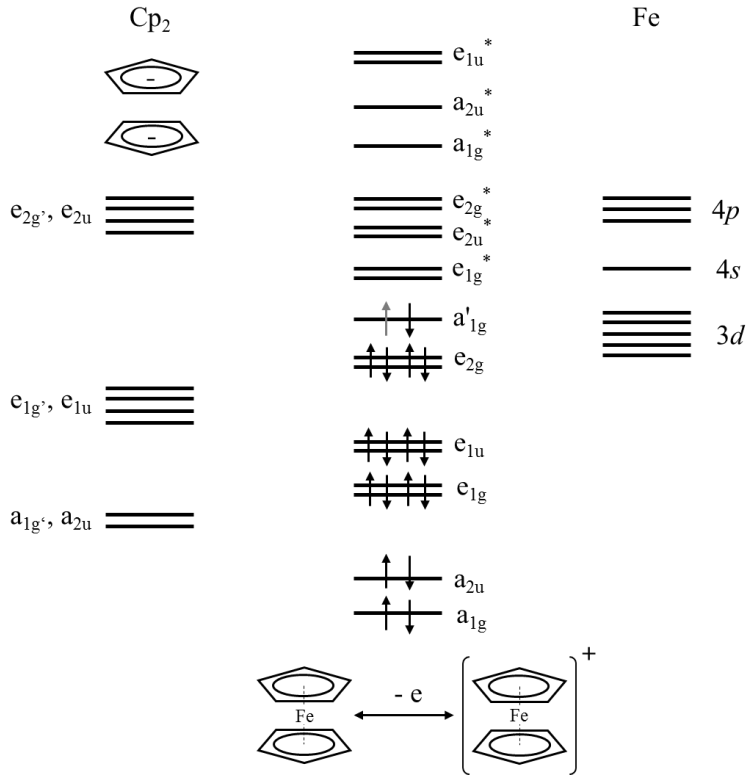

Fig. 39 Molecular orbital of ferrocene

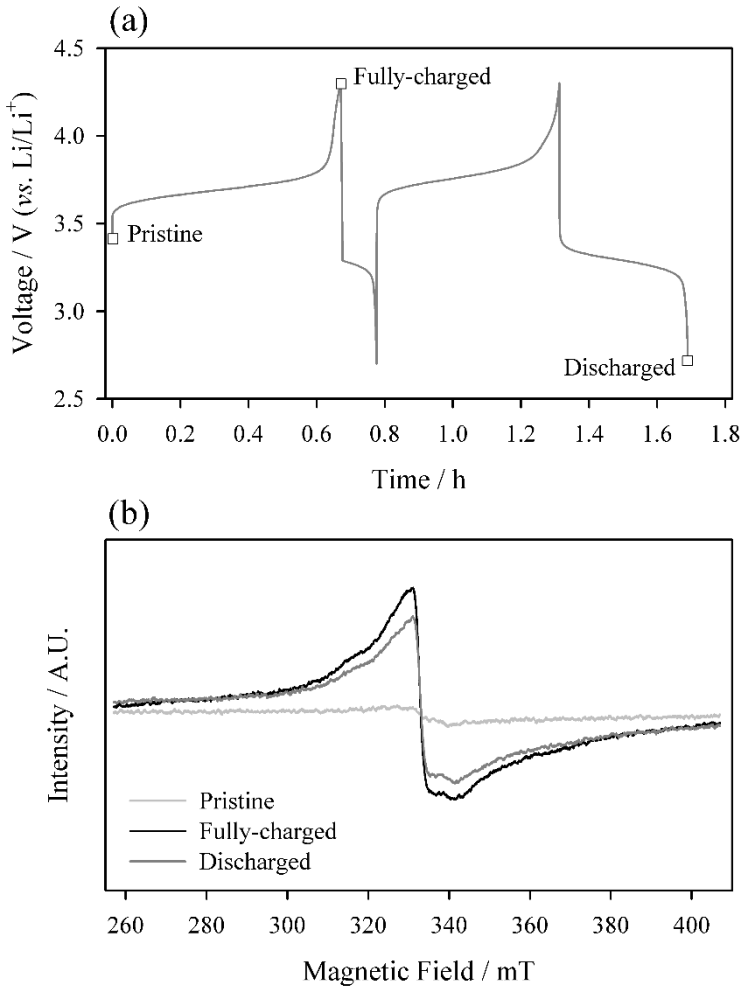

Fig. 40 (a); time *vs.* voltage curves of 10 m*M* AcFc dissolve 1.0 *M* $LiPF_6$ in PC supporting electrolyte at H-cell and (b); ESR spectra of AcFc dissolved electrolyte measured at -150 ℃ *C*-rate = 0.2 *C* CC, voltage cut-off = 2.7 V to 3.8 V (*vs.* Li/Li^+).

because unpaired electron is not exist at AcFc. After 1st charging, the $AcFc^+$ is electrochemically generated. Therefore, the intense ESR signal is observed from unpaired electron in $AcFc^+$ molecule. The irreversible capacity after 1st charging is from the electrolyte extraction from H-cell. Since the AcFc is electrochemically regenerated after 2nd discharging, the reduced intensity from $AcFc^+$ is obtained from ESR. In short, the electrochemical charge-discharge mechanism of AcFc is as expected from cyclic voltammogram. Furthermore, the SOC of AcFc electrolyte is easily traced by ESR measurement.

5. Conclusion

The electrochemical and physicochemical properties of several nitrogen-containing molecules and metallocene derivatives are enhanced by structural modification. Nitrogen atom have lone pair electrons, which is applicable as ligand and redox center; thereby applying as redox couple design. Moreover, the negative charged nitrogen atom is nucleophile, resulting readily functional group substitution by S_N2 reaction. Thus, nitrogen atom is applied as ligand molecule, redox center and the attachment center of aliphatic group for structural modification of redox couples. While non-aqueous flow battery is highlighted by its energy density from wide electrochemical stability window of organic electrolyte, the solubility drawback is remained problem for practical application of non-aqueous system. Since the nitrogen can be applied with diverse manner for molecule design, the limitation of solubility can be resolved by rational design of nitrogen-containing redox couples.

i) An azamacrocyclic ligand, 1,4,8,11-tetraazacyclotetradecane (cyclam) is firstly demonstrated as a single redox couple for non-aqueous flow batteries. Single redox couple has advantageous feature for practical application because permanent loss of active material from cross-contamination at dual electrolyte-comprised cell is completely prevented. The energy density of this complex cation is tailored by counter anions and composition of supporting electrolytes. The enhanced cell voltage and solubility (volumetric capacity) are concluded by weak-coordinating anions, which is easily dissociative in high dielectric solvents. Further enhanced solubility is achieved by increasing dielectric constant of supporting electrolyte. The optimized composition

of nickel(II)-chelated complex cation demonstrates high solubility (0.8 *M*) and working voltage (2.55 V), resulting energy density of 27.3 W h L^{-1}.

ii) Nitrogen atom is applied as redox center in *p*-phenyldiamines (PD) as positive redox couple. Two amine groups (-NH_2) in PD offer two-step redox reactions at single molecule; that is, delivered capacity from PD is twice than conventional redox couples at same concentration, ensuring cost-advantages. However, the solubility and chemical/electrochemical stability drawbacks are bottle-neck for flow battery applications in PD. The methylation of amine groups enhances both two problematic properties. The ten-fold increase in solubility (5.0 *M*) and decrease in melting point are due to the elimination of hydrogen bonding from methylation of PD. The solubility equation clearly indicates that the solubility can be influenced by depression of melting points. The chemical and electrochemical stability of PD molecule is improved by methyl substitution, which is the expected result from the sterically hindered nitrogen redox center. Fully-methylated *N*,*N*,*N′*,*N′*-tetramethyl-*p*-phenylenediamine (TMPD) demonstrates high energy density with 938.0 W h L^{-1}, which is from 5.0 *M* of solubility and 3.2 and 3.8 V (*vs*. Li/Li^+) of working voltages. Moreover, TMPD has highly stable electrochemistry and facile mass transfer; therefore, the use of TMPD as flow battery electrolyte is promising from its excellent electrochemical and physicochemical performances.

iii) Butyl-substituted, *N*-butylphthalimide (BPI) is suggested as negative redox couple

for non-aqueous flow batteries. The ten times enhancement of solubility (5.0 *M*) and depression of melting point are from the asymmetric molecular structure by attaching butyl groups on nitrogen atom. Again, the strong relationship between maximum solubility and melting point implies this result. The electron-donating and solvation effect of butyl groups lifts the redox potential (0.1 V), which is desirable for energy density of flow batteries. The butyl-subsitution on phthalimide is bifunctional; these are, voltage lift (0.1 V) by upstream-shift of LUMO and increase of solubility (5.0 *M*). Finally, BPI/TMPD full cell demonstrates promising behavior as all-organic flow batteries; resulting 120.6 W h L^{-1} of energy density.

In short, the energy density of non-aqueous flow batteries are greatly improved by introduction of the nitrogen-containing molecules. The correlation between solubility and melting point is applied as excellent rule-of-thumb for designing highly soluble redox couples. The theoretical energy density of three-types of flow battery systems exceeds 25.0 W h L^{-1}, which is the typical energy density of all-vanadium redox flow battery system. The ideal solubility equation can be applied as design principle; for instance, the ferrocene-based positive redox couple in this study.

References

[1] M. Armand, J.M. Tarascon, Nature 451 (2008) 652-657.

[2] H.S. Chen, T.N. Cong, W. Yang, C.Q. Tan, Y.L. Li, Y.L. Ding, Prog. Nat. Sci. 19 (2009) 291-312.

[3] M. Skyllas-Kazacos, L. Cao, M. Kazacos, N. Kausar, A. Mousa, ChemSusChem 9 (2016) 1521-1543.

[4] K. Xu, Chem. Rev. 104 (2004) 4303-4418.

[5] A. Posner, Fuel 34 (1955) 330-338.

[6] K. Gong, Q. Fang, S. Gu, S.F.Y. Li, Y. Yan, Energy Environ. Sci. 8 (2015) 3515-3530.

[7] W. Wang, Q. Luo, B. Li, X. Wei, L. Li, Z. Yang, Adv. Funct. Mater. 23 (2013) 970-986.

[8] P. Singh, J. Power Sources 11 (1984) 135-142.

[9] J. Mun, M.-J. Lee, J.-W. Park, D.-J. Oh, D.-Y. Lee, S.-G. Doo, Electrochem. Solid-State Lett. 15 (2012) A80-A82.

[10] Q.H. Liu, A.E.S. Sleightholme, A.A. Shinkle, Y.D. Li, L.T. Thompson, Electrochem. Commun. 11 (2009) 2312-2315.

[11] A.A. Shinkle, T.J. Pomaville, A.E.S. Sleightholme, L.T. Thompson, C.W. Monroe, J. Power Sources 248 (2014) 1299-1305.

[12] Z. Li, S. Li, S. Liu, K. Huang, D. Fang, F. Wang, S. Peng, Electrochem. Solid-State Lett. 14 (2011) A171-A173.

[13] F.R. Brushett, J.T. Vaughey, A.N. Jansen, Adv. Energy Mater. 2 (2012) 1390-1396.

[14] K. Izutsu, Selection and Preparation of Supporting Electrolytes, in: Electrochemistry in Nonaqueous Solutions, Wiley-VCH Verlag GmbH & Co. KGaA, 2009, pp. 321-331.

[15] S.H. Yalkowsky, J. Pharm. Sci. 103 (2014) 2629-2634.

[16] M. Skyllas-Kazacos, F. Grossmith, J. Electrochem. Soc. 134 (1987) 2950-2953.

[17] R.F. Gahn, N.H. Hagedorn, J.S. Ling, DOE/NASA/12726-21 (1983).

[18] E. Sum, M. Skyllaskazacos, J. Power Sources 15 (1985) 179-190.

[19] G.L. Soloveichik, Chem Rev 115 (2015) 11533-11558.

[20] B. Sun, M. Skyllas-Kazacos, Electrochim. Acta 37 (1992) 1253-1260.

[21] B. Sun, M. Skyllas-Kazacos, Electrochim. Acta 37 (1992) 2459-2465.

[22] W.H. Wang, X.D. Wang, Electrochim. Acta 52 (2007) 6755-6762.

[23] M. Kazacos, M. Cheng, M. Skyllas-Kazacos, J. Appl. Electrochem. 20 (1990) 463-467.

[24] D.J. Eustace, J. Electrochem. Soc. 127 (1980) 528-532.

[25] C.P. de Leon, A. Frias-Ferrer, J. Gonzalez-Garcia, D.A. Szanto, F.C. Walsh, J. Power Sources 160 (2006) 716-732.

[26] Y. Matsuda, K. Tanaka, M. Okada, Y. Takasu, M. Morita, T. Matsumurainoue, J. Appl. Electrochem. 18 (1988) 909-914.

[27] R.R. Gagne, C.A. Koval, G.C. Lisensky, Inorg. Chem. 19 (1980) 2854-2855.

[28] H.-s. Kim, T. Yoon, Y. Kim, S. Hwang, J.H. Ryu, S.M. Oh, Electrochem. Commun. 69 (2016) 72-75.

[29] P.J. Elving, J.T. Leone, J. Am. Chem. Soc. 80 (1958) 1021-1029.

[30] W. Wang, W. Xu, L. Cosimbescu, D. Choi, L. Li, Z. Yang, Chemical Communications 48 (2012) 6669-6671.

[31] X. Wei, W. Xu, M. Vijayakumar, L. Cosimbescu, T. Liu, V. Sprenkle, W. Wang, Adv. Mater. 26 (2014) 7649-7653.

[32] Y. Zhao, Y. Ding, Y. Li, L. Peng, H.R. Byon, J.B. Goodenough, G. Yu, Chem. Soc. Rev. 44 (2015) 7968-7996.

[33] X. Wei, W. Xu, J. Huang, L. Zhang, E. Walter, C. Lawrence, M. Vijayakumar, W.A. Henderson, T. Liu, L. Cosimbescu, B. Li, V. Sprenkle, W. Wang, Angew Chem Int Ed Engl 54 (2015) 8684-8687.

[34] M. Duduta, B. Ho, V.C. Wood, P. Limthongkul, V.E. Brunini, W.C. Carter, Y.M. Chiang, Adv. Energy Mater. 1 (2011) 511-516.

[35] F. Pan, J. Yang, Q.Z. Huang, X.Z. Wang, H. Huang, Q. Wang, Adv. Energy Mater. 4 (2014) 1400567.

[36] J. Winsberg, T. Hagemann, S. Muench, C. Friebe, B. Häupler, T. Janoschka, S. Morgenstern, M.D. Hager, U.S. Schubert, Chem. Mater. 28 (2016) 3401-3405.

[37] T. Janoschka, N. Martin, U. Martin, C. Friebe, S. Morgenstern, H. Hiller, M.D. Hager, U.S. Schubert, Nature 527 (2015) 78-81.

[38] S.H. Oh, C.W. Lee, D.H. Chun, J.D. Jeon, J. Shim, K.H. Shin, J.H. Yang, J. Mater. Chem. A 2 (2014) 19994-19998.

[39] B. Bosnich, M.L. Tobe, G.A. Webb, Inorg. Chem. 4 (1965) 1109-&.

[40] C.A. Craig, L.O. Spreer, J.W. Otvos, M. Calvin, J. Phys. Chem. 94 (1990) 7957-7960.

[41] M.J.Frisch, et al., Gaussian 09 (Revision D.01), Gaussian Inc., Wallingford, CT, 2009.

[42] A.D. Becke, J. Chem. Phys. 98 (1993) 5648-5652.

[43] C. Lee, W. Yang, R.G. Parr, Phys. Rev. B 37 (1988) 785-789.

[44] S. Leroy, H. Martinez, R. Dedryvère, D. Lemordant, D. Gonbeau, Appl. Surf. Sci. 253 (2007) 4895-4905.

[45] R.I.R. Blyth, H. Buqa, F.P. Netzer, M.G. Ramsey, J.O. Besenhard, P. Golob, M. Winter, Appl. Surf. Sci. 167 (2000) 99-106.

[46] H. Senoh, M. Yao, H. Sakaebe, K. Yasuda, Z. Siroma, Electrochim. Acta 56 (2011) 10145-10150.

[47] V.J. Thom, C.C. Fox, J.C.A. Boeyens, R.D. Hancock, J. Am. Chem. Soc. 106 (1984) 5947-5955.

[48] M.R. Rosenthal, J. Chem. Educ. 50 (1973) 331.

[49] D. Lewis, E. Estes, D. Hodgson, J. of Crys. Mol. Struct. 5 (1975) 67-74.

[50] L. Simeral, R.L. Amey, J. Phys. Chem. 74 (1970) 1443-1446.

[51] A.J. Bard, L.R. Faulkner, Electrochemical Methods: Fundamentals and Applications, Wiley, 2000.

[52] J.A. Suttil, J.F. Kucharyson, I.L. Escalante-Garcia, P.J. Cabrera, B.R. James, R.F. Savinell, M.S. Sanford, L.T. Thompson, J. Mater. Chem. A 3 (2015) 7929-7938.

[53] G.S. Rohrer, Structure and bonding in crystalline materials, Cambridge University Press, 2001.

[54] M. Galiński, A. Lewandowski, I. Stępniak, Electrochim. Acta 51 (2006) 5567-

5580.

[55] D.H. Geske, A.H. Maki, J. Am. Chem. Soc. 82 (1960) 2671-2676.

[56] D.R. Rosseinsky, R.J. Mortimer, Adv. Mater. 13 (2001) 783-793.

[57] M. Armand, S. Grugeon, H. Vezin, S. Laruelle, P. Ribiere, P. Poizot, J.M. Tarascon, Nat. Mater. 8 (2009) 120-125.

[58] Y. Park, D.-S. Shin, S.H. Woo, N.S. Choi, K.H. Shin, S.M. Oh, K.T. Lee, S.Y. Hong, Adv. Mater. 24 (2012) 3562-3567.

[59] Y. Zhao, Y. Ding, J. Song, G. Li, G. Dong, J.B. Goodenough, G. Yu, Angew. Chem. 126 (2014) 11216-11220.

[60] I. Langmuir, Science 54 (1921) 59-67.

[61] P. Pyykkö, J. Organomet. Chem. 691 (2006) 4336-4340.

[62] R.L. Wang, J.R. Dahn, J. Electrochem. Soc. 153 (2006) A1922-A1928.

[63] Z.-G. Le, Z.-C. Chen, Y. Hu, Q.-G. Zheng, Synthesis 2004 (2004) 208-212.

[64] V. Gutmann, G. Gritzner, K. Danksagmuller, Inorg. Chim. Acta 17 (1976) 81-86.

[65] J.S. Jaworski, E. Leniewska, M.K. Kalinowski, J. Electroanal. Chem. Interfacial Electrochem. 105 (1979) 329-334.

[66] T. Liu, X. Wei, Z. Nie, V. Sprenkle, W. Wang, Adv. Energy Mater. 6 (2016) 1501449.

[67] X.L. Wei, L. Cosimbescu, W. Xu, J.Z. Hu, M. Vijayakumar, J. Feng, M.Y. Hu, X.C. Deng, J. Xiao, J. Liu, V. Sprenkle, W. Wang, Adv. Energy Mater. 5 (2015) 1400678.

[68] M. Bejblová, S.I. Zones, J. Čejka, Appl. Catal., A. 327 (2007) 255-260.

[69] R.H. Stokes, R.A. Robinson, J. Phys. Chem. 70 (1966) 2126-2131.

[70] R.J.C. Brown, R.F.C. Brown, J. Chem. Educ. 77 (2000) 724.

[71] K.L. Williamson, Macroscale and microscale organic experiments, D.C. Heath, 1989.

[72] S.-K. Park, J. Shim, J. Yang, K.-H. Shin, C.-S. Jin, B.S. Lee, Y.-S. Lee, J.-D. Jeon, Electrochem. Commun. 59 (2015) 68-71.

요약 (국문초록)

비수계 전해액의 넓은 전위창을 통하여 높은 작동 전압이 설계 가능한 비수계 흐름 전지의 상용화에 큰 장해요소인 에너지 밀도 문제를 해결하기 위하여, 본 연구에서는 질소를 포함하는 산화환원쌍의 분자 구조 개선을 통하여 전기화학적, 물리화학적 성질을 개선하였다. 질소 원자의 경우 옥텟 규칙을 만족할 때에, 비공유 전자쌍이 존재하여 금속 이온과 결합할 수 있는 리간드로 적용 가능할 수 있을 뿐만 아니라 이 비공유 전자쌍이 전기화학 반응을 통해서 산화환원 반응이 일어나는 산화환원 중심이 될 수도 있으며, 질소 원자 자체에 치환기를 부착하는 것이 용이하여 물질 설계의 여지가 다양하다는 점에서 큰 이점을 지닌다. 이러한 질소 원자의 다양한 화학적 성질을 하기 고-에너지 밀도를 지니는 3가지 산화환원쌍의 설계에 적용하였다.

첫 번째로, 질소 원자를 테트라-덴테이트 아자-거대고리 리간드의 구성요소로 적용하여 니클 2가 이온에 킬레이트 시킴으로써 비수계 흐름 전지용 단일 산화환원쌍을 설계하였다. 단일 산화환원쌍이 비수계 흐름 전지용 활물질로 적용되었을 때에는, 이종의 활물질이 각각 양-음극 전해액으로 적용되는 것에 비하여 상호 오염에 의한 영구적 활물질 손실이 없다는 점에서 큰 이점을 지닌다. 본 전이금속 착 양이온의 경우 거대 고리 리간드의 강한 킬레이트 효과로 인하여 높은 전기화학적, 화학적 안정성을 지닐 뿐만 아니라 해리가 용이하게 일어나는 결합력이 약한 이온 반경이 큰

음이온을 상대 음이온으로 적용하였을 때에 더욱 높은 에너지 밀도를 지닐 수 있었다. 이에 높은 유전상수를 갖는 에틸렌 카보네이트-프로필렌 카보네이트의 혼합 용매를 지지 전해질 용 용매로 적용하였을 때에 더 높은 부피 당 용량을 구현할 수 있었고, 최종적으로는 0.8 *M*의 용해도와 2.55 V의 작동전압을 통하여 27.3 W h L^{-1}의 에너지 밀도를 안정적인 수명특성과 함께 구현하였다.

두 번째로, 질소의 비공유 전자쌍을 산화환원 중심으로 적용하여 *p*-페닐렌디아민을 양극 전해액용 산화환원쌍으로 제시하였다. 이 유기 분자 내에 존재하는 두 아민 작용기는 두 전자가 관여하는 산화환원 반응을 가능케 하기에, 같은 농도의 전해액에서도 두 배의 용량을 구현할 수 있어 전지의 단가를 크게 절감할 수 있다는 특성을 지닌다. 그러나, 낮은 용해도 (0.5 *M*)와 화학적 가역성이 흐름 전지에의 적용에 문제시 되기에, 아민 작용기의 수소를 메틸로 치환하여 이 두 가지 문제점을 해결하고자 하였다. 메틸 그룹으로 모든 수소가 치환된 *N,N,N′,N′*-테트라메틸-*p*-페닐렌디아민 (TMPD)의 경우 10배의 양 (5.0 *M*)이 동일 전해액에 용해되었는데, 이는 수소 결합의 소멸에서 기인한 녹는점의 하락과 궤를 같이 하였다. 이는 이상 용액에서의 용해도 추정식에서 확인 가능한 녹는점과 용해도의 상관관계와 일치하는 결과이다. 뿐만 아니라, 치환시킨 메틸 작용기를 통하여 산화환원 중심인 질소 원자에의 입체 장애 효과를 증대시켜, 생성되는 라디칼 및 양이온의 안정성을 증대시킬 수 있었다. 이와 같은

메틸 치환의 두 가지 효과를 통하여 938.0 W h L^{-1}의 에너지 밀도를 지니는 흐름 전지용 양극 전해액을 설계할 수 있었고, TMPD의 경우 유기 전해액 내부에서의 빠른 확산을 통하여 출력 특성이 높은 전지 또한 설계할 수 있음을 알 수 있었다.

마지막으로, 부틸이 치환된 프탈이미드 소재인 *N*-부틸프탈이미드 (BPI)를 비수계 흐름 전지용 음극 산화환원쌍으로 설계하였다. 기존에 보고된 *N*-메틸프탈이미드에 비하여 부틸 작용기가 질소 원자에 부착되었을 때에, 길어진 탄화수소 사슬로 인한 비대칭성으로 녹는점이 하강되어, 10배가 향상된 용해도 (5.0 *M*)를 달성할 수 있었다. 뿐만 아니라 부틸 작용기의 더 높아진 전자 주개 효과와 용매화 개선 효과로 프탈이미드의 환원이 더 어려워지고, 이로 인하여 음극의 작동 전압이 0.1 V 더 낮아져 음극 산화환원쌍으로 더욱 적합한 고-에너지 밀도 소재를 설계할 수 있었다. 최종적으로 TMPD를 양극으로, BPI를 음극으로 적용한 전-유기계 흐름 전지에서 안정적인 충방전 거동을 확인할 수 있었고, 이러한 산화환원쌍 조합을 통하여 120.6 W h L^{-1}의 이론 에너지 밀도를 달성할 수 있었다.

주요어: 리독스-흐름 전지; 산화환원쌍; 비수계 전해액; 용해도; 에너지 밀도; 전기화학 성능

학 번: 2012-22582